Applications of Superconducting Re-Entrant Microwave Cavities

by

Thomas Jerry Clark

A thesis submitted in partial fulfillment of the requirements for the degree of

Master of Science

Department of Physics

University of Alberta

Abstract

This thesis describes the design, fabrication, and characterization of 3D superconducting microwave cavities for two applications. It first describes a cryogenically compatible microwave filter that is able to tune its resonant frequency by an unprecedented 5 GHz via deformation caused by a a helium pressure vessel. Then, it describes a novel microwave optomechanics device where such a cavity is coupled to an aluminized SiN membrane. It demonstrates that this device can be back-action cooled from the 450 mK base temperature of the cryostat down to 160 mK.

Acknowledgements

Throughout my time as a graduate student at the University of Alberta, I have received support and assistance from many people, and I am immensely grateful for it.

I would like to first thank my supervisor, Dr. Davis, for cultivating a work environment where new ideas are able to take shape and grow. One where science is exciting, and where it always feels like it's just one day away from your new idea working. I'm deeply indebted to Greg Popowich for his levelheadedness, constant willingness to help, and his depth of knowledge that he's always willing to share. I'm thankful to the post-docs that I've had the pleasure of working with: to Fabien for his patience and positivity when working through hard problems, and to Vaisakh for his fresh perspectives and willingness to, and uncanny speed at, slugging through unfamiliar material. By just watching the way you do things I've learned a lot about how science is done well. I'm equal parts grateful to, and jealous of the senior members of the lab, who never fail to impress me with their knowledge and the ease with which they solve insurmountable problems. Brad, Allison, Paul, and Callum: thank you for all of the interesting discussions and help over the years. I always learn something when I get the change to talk to you. I'm eternally appreciative of the time I got to spend with the less-senior grad students like me. Hugh, Clinton, Alex, Holly (close enough to a grad student): I can't think of better people to have had the chance to work so closely with over the past couple years. I'd be remiss if I didn't acknowledge my friends outside of the lab: thank you for being there for the study sessions, the wild adventures, and the late nights (both work and play). Aaron, Corbin, Julie, Katelyn, everyone else: I wouldn't have made it without you. I'm thankful to my girlfriend, Astrid, for her unfailing ability to make me laugh, and for making me better. Finally, I can't even express how thankful I am for family. Their unwavering support and love has been a constant source of inspiration and comfort.

You've all made an indelible mark on my life, and I wouldn't be the same person or scientist I am without your presence in my life. Thank you.

Contents

Abstract ii

Acknowledgements iii

List of Figures viii

List Of Acronyms x

1 Introduction **1**

1.1 Summary of Thesis 2

2 Extremely Tunable Filter Cavity **3**

2.1 Tunable Re-Entrant Cavities 4

2.1.1 Tuning Mechanism 7

2.1.2 Deformation Mechanism Toy Model 7

2.1.3 Capacitance Change Toy Model 7

2.1.4 Quantitative Model 8

2.1.5 Quality Factor 11

2.2 Input-Output Coupling 12

2.3 Scattering Parameters 13

2.3.1 Notch Geometry 14

2.3.2 Transmission Geometry 14

2.3.3 Reflection Geometry 15

2.4 Input-Output Coupling : Analytical Methods 15

2.5 Input-Output Coupling: Simulations 16
2.6 Fabrication 18
2.7 Refrigeration 19
2.8 Cavity Measurements 20
2.9 Phase noise 24
2.10 Phase Noise measurement 25
2.10.1 Input Signal 27
2.10.2 Splitter Output 27
2.10.3 Introduction of Delay 27
2.10.4 Mixer Output 28
2.10.5 Filter Output 28
2.10.6 Quadrature Assumption 29
2.10.7 Mixer Inputs In Quadrature 31
2.10.8 Small Signal Assumption 31
2.10.9 Transfer Function 32
2.11 Results 33
2.12 Conclusion 34

3 Microwave optomechanics **36**

3.1 A Post Cavity Implementation 37
3.1.1 Microwave Cavity 37
3.1.2 Mechanical Resonator 38
3.2 Analytical Optomechanical Coupling for A Re-Entrant Membrane Cavity 39
3.3 Refrigeration 41
3.4 Cavity Characterization 41
3.4.1 Microwave Cavity Measurements 41
3.4.2 Mechanical Measurements 42
3.5 Optomechanical Cooling 47

3.6 Conclusion 49

4 Conclusion **51**

4.1 Summary 51

4.2 Next Steps 52

Bibliography **53**

List of Figures

2.1 COMSOL simulations for the electric and magnetic fields inside re-entrant microwave cavities. 5

2.2 Coupling geometries for a two port cavity. 13

2.3 Coupling from a coaxial waveguide to a cavity eigenmode. 16

2.4 Simulation details for determining coupling to a re-entrant cavity. . . 17

2.5 Exploded view of the tunable filter cavity. 19

2.6 Photographs of the cryostat and how our cafity is affixed to it. 20

2.7 Measurement schematic and typical dataset for determining quality factor and center frequency of tunable filter. 21

2.8 The tunable filter's normalized amplitude response at a variety of pressures. 22

2.9 The filter quality factor and center frequency as a function of pressure. 23

2.10 Demonstration of phase noise in a mock signal. 25

2.11 Graphical representation of phase noise filtering 26

2.12 Schematic of a delay line discriminator 26

2.13 Mock transfer functions demonstrating the effect of different delay line lengths. 34

2.14 Detailed measurement schematic and measurement results for phase noise filtration of a commercial microwave source 35

3.1 Schematic of the membrane element and associated FEM simulation . 38

3.2 Photograph of the optomechanical device. 39
3.3 Measurement schematic and data for characterization of the microwave properties of the device. 42
3.4 Measurement schematic and data for characterization of the microwave properties of the device. 44
3.5 Simulation details for determining the effective mass of the aluminized membrane. 46
3.6 Demonstration of sideband cooling. 48

List Of Acronyms

FEM Finite Element Method

VNA Vector Network Analyzer

Si Silicon

SiN Silicon Nitride

MEMS Micro-Electro-Mechanical Systems

Chapter 1

Introduction

This thesis describes the development of superconducting 3D microwave cavities for cryogenic filtering and for microwave optomechanics. This work is motivated by the enormous progress in cavity quantum electrodynamics and optomechanics recently made through use of 3D cavities like the ones described in this thesis.

3D Microwave cavities have recently become integral components in the development of new technologies in a variety of fields. For example, they been shown to enable unprecedentedly long coherence time transmon qubits [1], optomechanical systems in the strong coupling regime [2], hybrid systems that convert signals from microwave to optical frequencies [3, 4, 5]. Their high quality factors and ease of integration with a variety of interesting systems make them an attractive and exciting tool.

Filters are a ubiquitous technology, and although 3D cavities are well suited as filters due to their potentially high quality factors, ease of cryogenic integration, and straightforward machining, they are only one of the possible implementations at cryogenic temperatures. Printed circuit board approaches [6, 7, 8], as well as elegant methods using waveguides as simple as a shielded twisted pair [9, 10] also exist, but these implementations tend to enable ease of miniaturization at the either expense of

manufacturing and design complexity or filter narrowness. Employing superconductors allows for sharp reduction of surface resistance at microwave frequencies, which allows for higher quality factors and narrower filters [11, 12]. Filter tunability is often desired to allow for a single filter to be used to multiple applications, as well as to fine tune the filter frequency to the application at hand. Much attention has been paid to the tunability of microfabricated and printed circuit board filters [13, 14, 15, 16, 17] due to the high demand for miniturization in conjunction with well established fabrication techniques. This thesis pursues an option that sacrifices miniaturization to instead focus on filter narrowness and large tunability.

The thesis will be organized as follows:

1.1 Summary of Thesis

Chapter 1 has briefly outlined the motivation for studying systems like the ones shown in this thesis.

Chapter 2 describes a novel implementation of a microwave cavity that enables very large tunabilities of the cavity frequency at cryogenic temperatures using a pressure vessel of helium to deform the cavity.

Chapter 3 describes a novel microwave optomechanical system developed for this thesis that couples a metallized SiN membrane to a microwave cavity.

Chapter 4 summarizes the results and gives some thoughts regarding future directions.

Chapter 2

Extremely Tunable Filter Cavity

This chapter will outline the design, simulation and measurement of a cryogenic microwave resonator capable of tuning its original 8 GHz resonance frequency by more than 5 GHz without serious degradation of its quality factor. Tunable cryogenically compatible cavities have been designed before using piezoelectric [18, 19], dielectric [20], mechanical [21], or MEMS-based [22] tuning elements, but each of these has drawbacks that make them less attractive. Piezoelectric crystals suffer from greatly reduced range at low temperatures, a macroscopic mechanical solution as proposed in [20, 21] requires expensive and bulky cyogenically compatible actuators, and a MEMS-based approach is expensive and time consuming to implement. This solution leverages deformation of a microwave cavity by a pressurized volume of helium, which is inherently crogenically compatible with no loss of efficacy and requires only standard machining processes.

The chapter will begin by considering the properties of a particular type of microwave cavity: The re-entrant post cavity. I will derive both toy and quantitative models for how such a cavity can be deformed to tune its resonant frequency, then show how coupling to this type of cavity can be simulated using a commercial finite element method solver. I will then describe the fabrication details of the cavity and

outline the measurement scheme I used to experimentally determine its quality factor center frequency.

I will conclude the chapter with a demonstration of the cavity as a phase noise filter, which necessitates first some explanation of phase noise and its measurement, then of our particular measurement apparatus.

2.1 Tunable Re-Entrant Cavities

Microwave cavities contain capacitive and inductive sub-components that allow for the storage of energy in electric and magnetic fields. These cavities can be constructed in a myriad of ways, from lumped elements on a circuit prototyping board, to reflectors made from vias on a printed circuit board [6], to the klystrons used to accelerate beams of particles to relativistic speeds [23].

Although the details of the fields in these resonators vary as widely as their geometry, all implementations will resonate with a frequency governed by:

$$\omega = \sqrt{\frac{1}{LC}}, \tag{2.1}$$

where L is the total inductance and C is the total capacitance [24].

This chapter will begin with the description of one such implementation: The 3D re-entrant cavity, which has recently been demonstrated to be a powerful tool in cavity electrodynamics where it has been leveraged for a variety technologies such as the creation of long coherence time quantum memories [1], the demonstration of bidirectional frequency conversion via coupling to ferrimagnetic spheroids [3], and the implementation of universal gate sets on qubits [25].

There are two significant geometrical regimes for post cavities, but in order to understand them most clearly, some terminology needs to first be introduced. For the length of this thesis, I'll be referring to directions within the cavity using the

language of cylindrical coordinates, where in Fig 2.1 the radial direction runs left to right within a cavity and the vertical direction runs up and down. A radial (vertical) face is one who's normal is in the radial (vertical) direction. I will be constantly referring to some critical geometrical elements, so I'm going to give them names here. The central protrusion extending from the lowest vertical face into the cavity volume can be called the stub or the post interchangeably. The highest vertical face is called the cap or the lid, a name inspired by how I have constructed these cavities. The cavity volume pinched between the vertical faces of the cap and the stub is called the gap, which as we will see is a critical design feature of this type of cavity. With this nomenclature, we can turn our attention to the different geometric regimes.

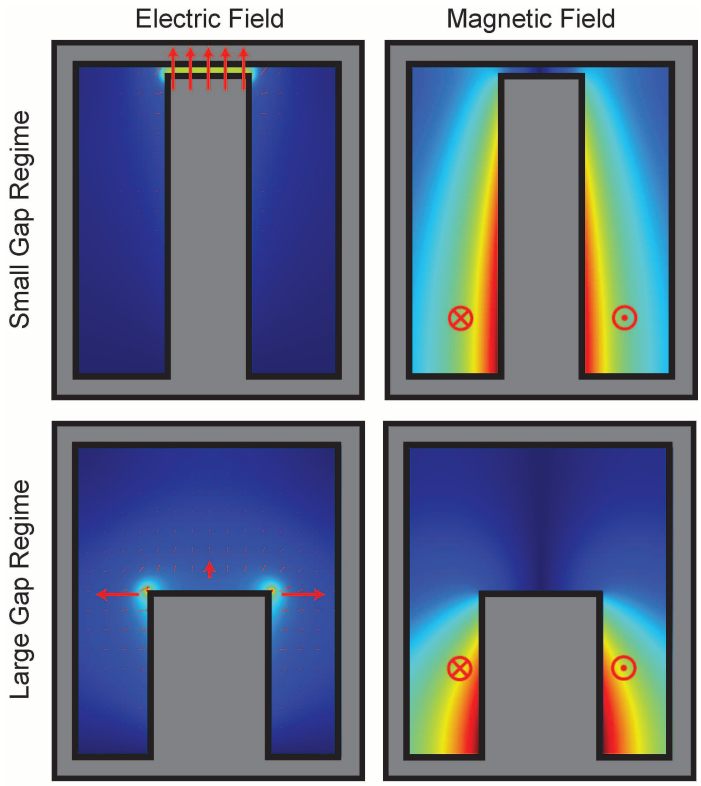

Figure 2.1: Finite element method (FEM) simulations of the electric and magnetic fields in the small and large gap regimes. The electric field in the small gap regime is highly localized in the gap, whereas in the large gap regime it is localized in a ring around the edge of the stub, and extends radially toward the wall. The magnetic field in both regimes in qualitatively identical, with the field circulating about the stub and decreasing in magnitude radially and along the length of the stub.

The first regime is characterized by having the dominant capacitance of the cavity caused by contributions between the radial face of the post and the radial cavity outer wall. In this regime, the gap between the vertical face of the post and the vertical face of the cavity lid is large. This regime is characterized by lowest order modes exhibiting a magnetic field circulating about the post, and an electric field flowing from the stub radially to the wall. Cavities in this regime have been used to great effect in developing 3D transmon qubits with long coherence times [1]. This regime is attractive not only due to its potential for extremely low losses, but also due to its similarities with a coaxial waveguide with open circuit termination, which permits analytical analysis of its resonant frequencies and fields. In this regime, due to the negligible effects of the metallic cap, the cap can be omitted entirely (leaving the uppermost "face" of the cavity to be air) with only minor perturbation to the cavity eigenmode. This approach can allow open access to the cavity volume and the fields therein: a potentially useful feature.

The second regime is where the gap between post and the metallic lid of the cavity grows small, and the capacitance contained between the lid and closest face of the post becomes large. In this regime the magnetic field still circulates about the stub, but the electric field becomes highly localized between the stub and lid. This dominating capacitance is the enabling feature of much of the technology outlined in this thesis: as the gap size is perturbed by some mechanism, this dominant capacitance is modified, which causes a shift in the cavity's resonance frequency. This frequency tunability can be useful in and of itself, as demonstrated by the phase noise filtration of this chapter, but it can also be used as an enabling factor for the implementation of various optomechanical systems, as will be shown in the next chapter.

Finite element simulations of these two regimes are displayed in Fig. 2.1, demonstrating the character of the electric and magnetic fields in this type of cavity.

2.1.1 Tuning Mechanism

Due to the central importance of cavity frequency changes caused by perturbations to the gap size for the technologies in this thesis, I'll take some time here to develop both an intuitive and a quantitative understanding of them. In either case, two things will need to be developed: A model for the mechanism of deformation, and a formula for the resonant frequency of a cavity that accounts for the effect of the changing gap size.

I'll start by developing a toy model for both of these, then improve the sophistication of the models and derive a quantitative formula for our specific experiment.

2.1.2 Deformation Mechanism Toy Model

A conceptually simple way to change the gap size would be to apply a uniform pressure to the top of the cap and deform it toward the stub. As a first approximation, we can pretend that there is no spatial dependence to the deformation and that the lid is an elastic material such that the deformation is given by:

$$x = \frac{F}{k} = \frac{P \cdot A}{k}, \tag{2.2}$$

where x is the displacement, $F = P \cdot A$ describes the force caused by our imaginary uniform pressure being applied over the area of our cap, and k is the spring constant of the cap. With this in hand, we can turn our attention to understanding how this simplified deformation affects the cavity frequency.

2.1.3 Capacitance Change Toy Model

Roughly, the capacitance of the post-lid gap can be approximated as a parallel plate capacitor, with capacitance $C = \frac{\epsilon A}{d}$. We can mathematically model the changing gap

caused by the uniform pressure we considered in the last section by introducing the displacement, x, into this equation as:

$$C = \frac{\epsilon A}{d_0 - x}. \tag{2.3}$$

The resonant frequency of a microwave resonator is given by $\omega = \frac{1}{\sqrt{LC}}$. By substituting in the expression for a parallel plate capacitor, one arrives at:

$$\omega \approx \sqrt{\frac{d_0 - x}{AL\epsilon}}. \tag{2.4}$$

By inspection of this equation, it is clear that the changing gap affects the resonant frequency, taking the derivative gives us information about the regime in which the chance is most rapid:

$$\frac{\partial\,\omega}{\partial\,x} = -\frac{1}{2\sqrt{AL\epsilon \cdot (d_0 - x)}}. \tag{2.5}$$

From this simplified equation, one can see that as the gap becomes very small (x becomes close to d_0) the cavity resonance frequency becomes more sensitive to further displacements. This motivates the use of very small gap sizes to maximize tunability given limited deformation.

This simple model is useful to develop intuition, but does not allow for accurate quantitative analysis. In order to more carefully understand the changing resonant frequency, we can turn to the analytical model.

2.1.4 Quantitative Model

We can begin our quantitative model by casting a more critical eye at our equation for the resonance frequency of a post cavity.

Quantitative Post Cavity Resonance Frequency

The analytic expression for a post cavity, called a klystron cavity in the context of the original paper, can be derived through the used of Green's functions methods [26]. The details are beyond the scope of this thesis, but when the dust settles the frequency is given by:

$$\omega_c = \frac{1}{2\pi}\sqrt{\frac{\mu_0\epsilon_0}{r_{\text{post}}h\left(\frac{r_{\text{post}}}{2d} + \frac{2}{\pi}\log\left(\frac{el_m}{d}\right)\right)\log\left(\frac{r_{\text{cav}}}{r_{\text{post}}}\right)}}, \tag{2.6}$$

where r_{post}, r_{cav}, and h are the radius of the post, the radius of the cavity, and the height of the cavity respectively. l_m is a purely geometric factor, given for our geometry by $l_m = 0.5\sqrt{(r_{\text{cav}} - r_{\text{post}})^2 + h^2}$, and e is Euler's constant.

Before blindly advancing with this equation in hand, it is instructive to pause to re-iterate some of the assumptions made in its derivation to ensure our conclusions and subsequent designs are reasonable. In order for the above expression to be valid, our cavity must satisfy:

1. l_M/λ_0 is small. This is a statement that the cavity size needs to be on the order of the vacuum wavelength.

2. r_{post}/l_M is not too small. This is a statement that the post must take up a significant part of the cavity volume. If the post is exceedingly small, the formula becomes inaccurate

The COMSOL simulations of Fig. 2.1 suggest that a centimeter scale cavity has frequencies on the order of 1 GHz, implying a vacuum wavelength on the order of 10s of centimeters, satisfying the first condition. Comparison to some of the example cavities given in [26] suggests that we should expect to satisfy the second to a reasonable extent.

Plate Deformation

Armed with this more precise equation for post cavities in our small gap regime, we can now turn to more carefully accounting for the effects of the changing gap. If the circular lid of the cavity is deformed by a pressure that is constant over the area of the lid, and the deformation is relatively small with respect to the thickness of the lid, we can model the lid as a circular plate with uniform loading and fixed support boundary conditions. The deformation of such a system is given by [27]:

$$w(r) = \frac{Pr_0^2}{64D}\left[1 - \frac{r^2}{r_0^2}\right]^2, \tag{2.7}$$

where $w(r)$ is the displacement from the undeformed plane of the plate, P is the applied pressure, r is the radial distance from the center of the plate and, r_0 is the radius of the plate. D is the flexural rigidity, a purely material property given by:

$$D = \frac{Et^3}{12(1-\nu^2)}, \tag{2.8}$$

where E, t, ν are the Young's Modulus, thickness, and Poisson's ratio respectively.

In order to approximate the capacitance of a capacitor with one of its walls deformed in this way, we can compute the average displacement caused by a pressure as:

$$\overline{d} = \frac{1}{\pi r_0^2}\int\int \frac{Pr_0^2}{64D}\left[1 - \frac{r^2}{r_0^2}\right]^2 \delta A = \frac{Pr_0^2 2\pi}{\pi r_0^2 64D}\int_0^{r_0}\left[r - \frac{r^3}{r_0^2}\right]\cdot \delta r = \frac{Pr_0^2}{128D}. \tag{2.9}$$

The important take-away from this equation is that the average deformation is linear with applied pressure. This means that the average gap size as a function of pressure can be written as:

$$d = d_0 - XP, \tag{2.10}$$

where X is a sensitivity parameter that describes how much the average gap changes as a function of applied pressure, defined above as:

$$X = \frac{r_0^2}{128D}. \tag{2.11}$$

X depends only on geometry and material properties, which makes it a useful figure of merit for how sensitive a given plate is to applied pressure.

By inserting this expression into the expression for resonant frequency, we arrive at the final functional form for the frequency of our cavity:

$$\omega_c = \frac{1}{2\pi}\sqrt{\frac{\mu_0\epsilon_0}{r_{\text{post}}h\left(\frac{r_{\text{post}}}{2(d-XP)} + \frac{2}{\pi}\log\left(\frac{el_m}{(d-XP)}\right)\right)\log\left(\frac{r_{\text{cav}}}{r_{\text{post}}}\right)}}. \tag{2.12}$$

With this understanding of how our filter's frequency response will shift as a function of pressure, we can turn our attention to a critical parameter of all oscillators: the quality factor.

2.1.5 Quality Factor

One of the main figures of merit for both cavities and filters is the quality factor. This parameter describes how damped a resonator is, with a higher quality factor indicating smaller damping. Quantitatively, the quality factor can be described by

$$Q = \omega \cdot \frac{\text{Energy Stored}}{\text{Energy Dissipated}}. \tag{2.13}$$

Many loss mechanisms can contribute to the overall damping of a resonator, and often it is convenient to describe their effects separately. The overall damping rate is given by:

$$\kappa_{\text{Total}} = \sum_n \kappa_n, \tag{2.14}$$

where κ_{Total}, κ_n refer to total damping rate and the damping rate caused by an individual, yet to be specified, loss mechanism respectively.

For the purposes of this thesis, it is sufficient to consider the total loss as a sum of two parts: The *external losses* that stem from energy leaking from the cavity into the ports we use to intentionally couple to our measurement apparatus, and the *internal losses* that arise due to processes internal to the cavity such as Ohmic losses. This conceptual splitting lets us write

$$\frac{1}{Q_{\text{total}}} = \sum_n \frac{1}{Q_{\text{n}}} = \frac{1}{Q_{\text{external}}} + \frac{1}{Q_{\text{internal}}} \tag{2.15}$$

There is a wealth of literature that describes the physical origin of the internal losses of microwave cavities. A particularly complete account is given in [28], but for the purposes of this thesis this simple separation will suffice.

A final important statement regarding the quality factor is its relation to linewidth in frequency space. A resonator with a large quality factor is sharp (has a small linewidth) in frequency space. Quantitatively, we can write:

$$Q = \frac{\omega_c}{\kappa}, \tag{2.16}$$

where ω_c is the cavity center frequency, and κ here take on the meaning of the full width half maximum linewidth of the Lorentzian cavity response.

2.2 Input-Output Coupling

In general, one can couple to a microwave cavity by exciting either the electric or magnetic fields. Commonly, this is achieved by the use of either an "antenna" coupler, or a "loop" coupler, which exchange energy with the electric and magnetic fields respectively. Antenna couplers usually consist of a small straight length of conductor

fed from a coaxial cable that either extends into the cavity volume (for large coupling rates) or is recessed into a cylindrical waveguide leading up to cavity volume (for smaller coupling rates). A schematic of an antenna coupler is shown in Fig. 2.3. Loop couplers are similar, but the length of conductor is bent into a physical loop and is electrically connected to the ground of the coaxial feed line. Fig. 2.4 shows a schematic of loop couplers, as well as some simulation details that will be discussed later in this chapter.

Each of these two coupler types can furthermore be arranged in three measurement geometries: Reflection, Transmission, or Notch. These geometries are shown in Fig. 2.2 below.

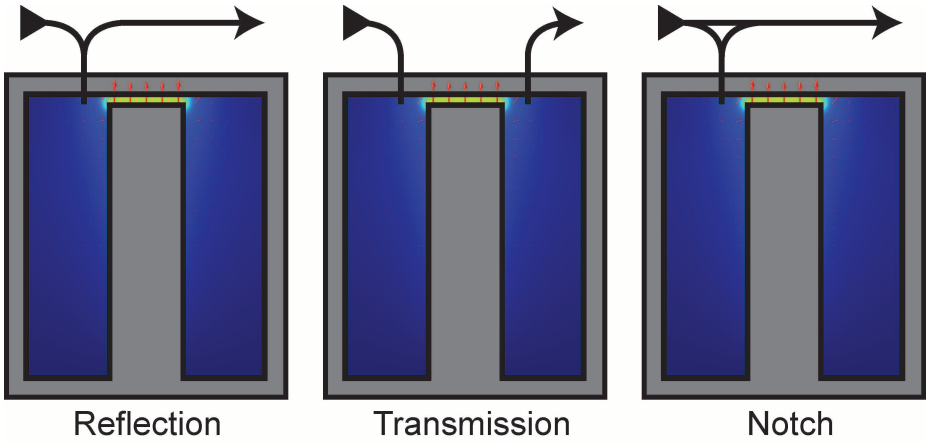

Figure 2.2: The three possible geometries for coupling to a two port cavity. The geometries are schematically shown with arrows indicating the flow of microwave power through the cavity, with details in the main text. It is important to note that each of these three have slightly different expressions for their scattering parameters, which is critically important when extracting the internal and external quality factors.

The differences between these geometries are outlined in brief below.

2.3 Scattering Parameters

A common tool in microwave engineering, which deserves brief mention here, is the idea of scattering parameters. Scattering parameters are values that relate the inci-

dent and reflected waves at each port of a microwave device [24]. They fully characterize the response of a microwave network to an applied microwave probe.

Fundamentally, the expressions for the scattering parameters can be derived from the lumped element models of their respective LC circuits, as in [29, 30], but for expediency only the final results and a reference for each are here stated.

2.3.1 Notch Geometry

The notch geometry is characterized by a continuous waveguide that passes by the cavity, with some mechanism allowing energy to be passed into and out of the cavity, such as via evanescent or inductive means, as described in [31]. The S_{12} scattering parameter of a notch cavity is given by:

$$S_{21}^{\text{Notch}}(f) = ae^{i\alpha}e^{-2\pi if\tau}\left[1 - \frac{Q_l/|Q_c|e^{i\phi}}{1 + 2iQ_l(f/f_r - 1)}\right], \tag{2.17}$$

where a, α, τ are parameters characterizing the influence of the external environment, encompassing the amplitude and phase shift of the measurement apparatus, as well as the cable delay respectively. Q_l, Q_c are the *loaded* and *coupling* quality factors, elsewhere in this thesis referred to as the *total* and *external* quality factors, f_r is the resonance frequency of the microwave cavity, and f is the frequency at which the cavity is being probed. Finally, ϕ characterizes the impedance mismatch between the coupler and the cavity.

2.3.2 Transmission Geometry

The transmission geometry is characterized by two separate waveguides that allow coupling to the cavity. In this geometry, the S_{12} Scattering parameter is given by [32, 31]

$$S_{21}^{\text{Transmission}}(f) = ae^{i\alpha}e^{-2\pi if\tau}\left[\frac{Q_l/|Q_c|e^{i\phi}}{1 + 2iQ_l(f/f_r - 1)}\right]. \tag{2.18}$$

This geometry, in contrast to the reflection case, has close to zero power flowing through the output port when the incident drive is off resonant. This is a useful feature for applications such as filtration, and will be the geometry we use for this chapter. This configuration comes with one serious detractor compared with the other two: due to the lack of a non-zero baseline, one can't separately determine Q_l and Q_c. This stems from the fact that the arbitrary constant describing the measurement apparatus, a, cannot be separated from $Q_l/|Q_c|$. In this topology, one can only derive Q_l from this measurement, and separate characterization of the reflection at each port is necessary to determine Q_c.

2.3.3 Reflection Geometry

A cavity in reflection has only one port, with the incident and reflected waves typically separated by external circuitry such as a circulator. In this geometry, the S_{11} scattering parameter takes a slightly different form. This is derived from [33] using the same form for the coupling to the environment as [31]:

$$S_{11}^{\text{Reflection}}(f) = ae^{i\alpha}e^{-2\pi i f\tau}\left[-1+\frac{\frac{2Q_l}{|Q_c|-Q_l}e^{i\phi}}{1+2jQ_l(f/f_r-1)}\right]. \tag{2.19}$$

2.4 Input-Output Coupling : Analytical Methods

When the coupler terminates before the volume of the cavity itself, the analysis developed by [28] can be applied. The coupler in this case can be thought of as first coupling from a coaxial waveguide to a cylindrical waveguide in cutoff, then subsequently coupling via an aperture into the cavity.

In the case of a cavity geometry that permits simple analytical forms for the electric and magnetic eigenmodes inside the cavity, such as the rectangular or cylindrical geometry, this can be used to find analytic formulas for the external quality factor.

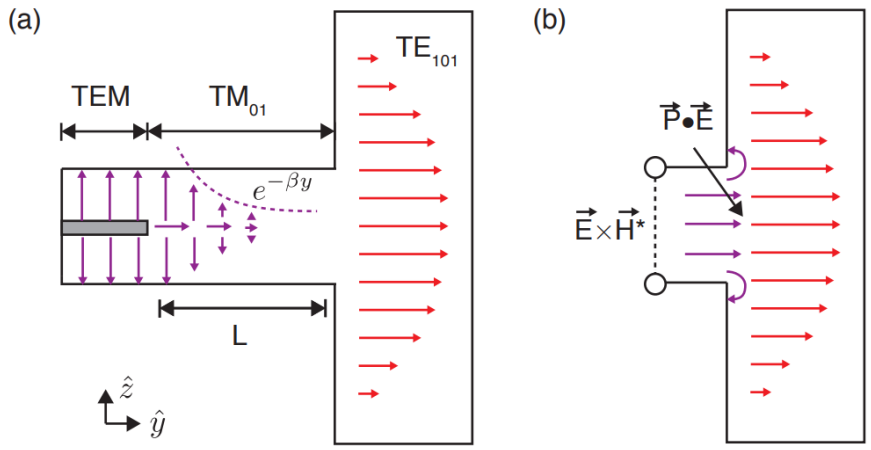

Figure 2.3: a) The coupling between the TEM mode of the coaxial waveguide to a circular waveguide. b) The subsequent aperture coupling from the cylindrical waveguide to the cavity body. Figure adapted from [28].

In our case, however, the field formulas are not straightforward and a numerical approach is preferable to determine how rapidly a given coupler will exchange energy with our cavity.

2.5 Input-Output Coupling: Simulations

Using the microwave waves package in COMSOL Multiphysics, the input output coupling can be simulated using the finite element method. This approach sidesteps the complicated analytical form of the mode inside the cavity and allows for rapid design of couplers.

The non-axisymmetric nature of the coaxial ports necessitate the use of a three-dimensional simulation. In order to extract the coupling strength, a frequency study can be used. Through fitting of the reflection coefficients as a function of frequency both the total and external quality factors can be determined.

In order to most closely determine the overall quality factor, the walls of the cavity body should be chosen to be impedance boundary conditions. This allows for Ohmic losses caused by finite resistivity. The coaxial port can be modeled as two concentric

metallic cylinders, with the annulus at their termination defined as a port boundary condition.

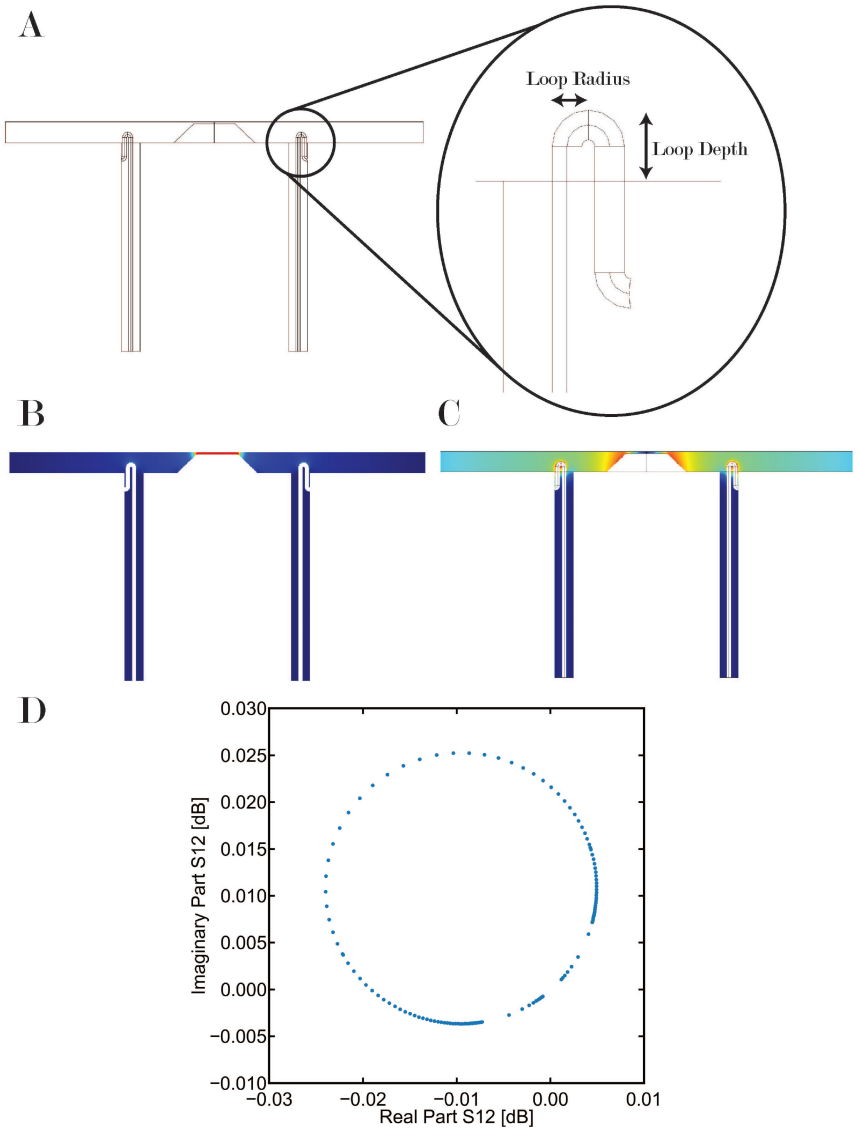

Figure 2.4: a) A wireframe view of the geometry used for calculating coupling to our microwave cavity. In this wireframe diagram, only the internal parts of the cavity are shown. The metal that encapsulates this shown volume is described by a boundary condition, and thus not included in the simulation volume. A detail view of the loop coupler is included, with the radius and depth of the loop coupler indicated. b) The electric field of the lowest order eigenmode of this cavity. The electric field is strongly localized in the small gap between the top of the cavity and the stub protruding into the cavity volume. c) The corresponding magnetic field of the lowest order eigenmode d) A sample nyquist plot produced by this simulation. This could be fit to Eq. 2.18 to extract the quality factors.

Two studies are carried out for a given cavity geometry. First, an eigenmode solver is run to yield the frequency of the resonance and to permit visual inspection of the modes. Once this center frequency is known, then a frequency study is run. This frequency study allows for the determination of the scattering parameters, which can be fit to determine the quality factors. The results of one such simulation is shown in Fig. 2.4. Once one is able to determine the quality factors at a given coupler depth, the depth of the coupler inside the cavity can be swept, and in this way the depth can be chosen to satisfy a condition of the designer's choosing. Looking forward to this cavity's application as a filter at the end of this chapter, I aimed to achieve maximum power throughput, which is achieved when the cavity satisfies both of $Q_{c,1} = Q_{c,2}$ and $Q_c = Q_0$.

2.6 Fabrication

Now that we have considered the fields in a stub cavity and the methods through which one can couple to it, we can shift our attention to actually implementing such a cavity. We fabricated the cavity in three parts. The microwave cavity itself is composed of two pieces of 6061 aluminium, a "body" and a "lid". These two pieces were fabricated on a lathe, then the body was sanded to reduce the gap between the lid and the stub to its final value of $\sim$100 μm. Two coupling waveguides (1.1 mm diameter) were drilled at a radial distance of 5mm from the center of the cavity to permit the introduction of couplers such that the cavity can be excited. Finally, both pieces were carefully polished to reduce losses stemming from contact resistance across the seam using brasso and a shop towel. The remaining piece of the cavity, which holds the volume of helium, was fabricated from multipurpose copper, and attached to the lid using an indium seal. An exploded view of the cavity design is shown in Fig. 2.5.

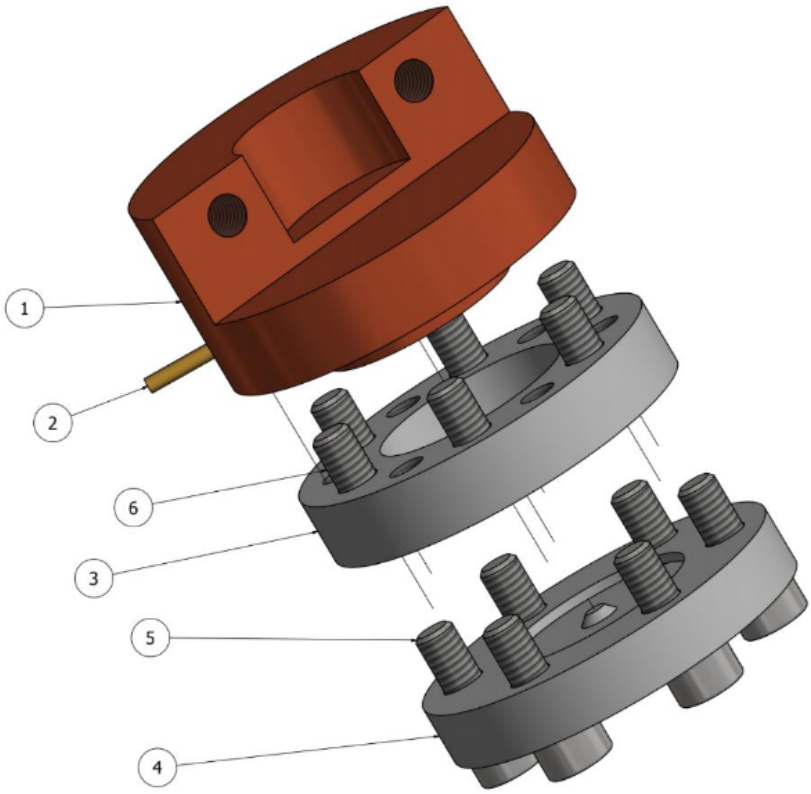

Figure 2.5: An exploded view of the cavity design. 1) is the copper mount to affix the experiment to the mixing chamber of our dilution refrigerator. 2) is the helium fill line, 3) is the deformable membrane, 4) is the re-entrant stub, 5) and 6) are standard screws. Adapted from personal correspondence with Dr. Fabien Souris.

2.7 Refrigeration

For this experiment, we rigidly affixed our cavity to the bottom of a dilution refrigerator. This system is interrogated through 40 dB of attenuation to thermally anchor the coax lines to each stage of the fridge. This refrigeration allows for the system to be probed well below the onset of superconductivity, which drastically improves the quality factor of the cavity. This improvement in quality factor is important for this application because it is related to the bandwidth of phase noise filtration, as will be explained in the coming sections. The base temperature of our dilution refrigeration

is ≈ 200 mK. In addition to the microwave measurement lines, we have also run a helium fill line to pressurize the volume of helium in the copper reservoir.

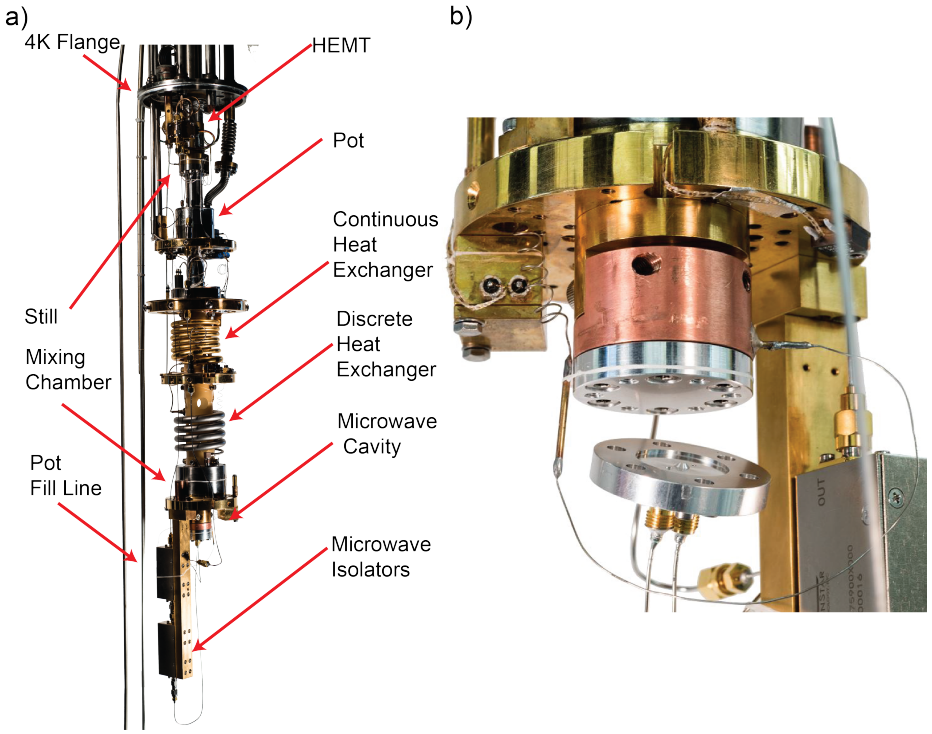

Figure 2.6: a) An image of the entire dilution system, with labels. b) A close-up image of the microwave cavity, open to expose the microwave cavity volume and the stub. The helium fill line to deform the cavity is visible soldered to the copper reservoir.

2.8 Cavity Measurements

The first set of measurements undertaken on this cavity are aimed at determining its quality factor and frequency as a function of applied pressure in the helium reservoir. These measurements consist of interrogation via a vector network analyser (VNA). This measurement apparatus allows for complete determination of the complex scattering parameters of our two-port cavity, which in turn allows for determination of our two figures of merit: the total quality factor and the cavity throughput.

In order to determine the quality factor, the cavity is probed with a VNA and the measurement is fit to the analytical formula for a transmission resonator in section

1.3. A typical measurement, along with a schematic of the VNA measurement scheme are shown in Fig. 2.7. In this measurement, the data is expressed in its complex form to facilitate fitting. It's important to note that this somewhat unintuitive form holds all the same information as the more familiar Lorentzian amplitude response and arctangent phase response.

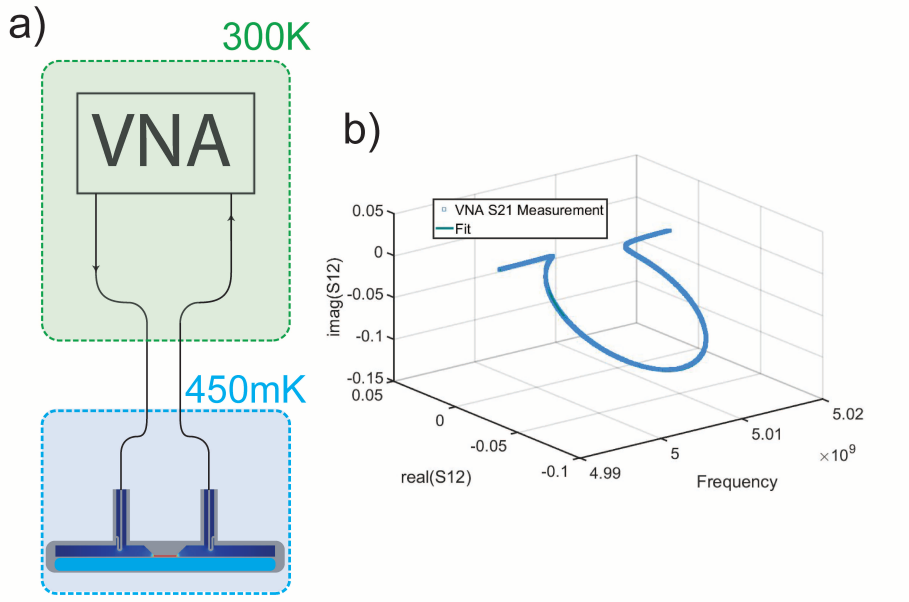

Figure 2.7: a) A schematic outlining the simplified measurement apparatus for determining the quality factor and resonance frequency as a function of applied pressure. b) A sample transmission measurement with its associated fit.

Once a single measurement can be taken and fit, we are able to demonstrate the tunability of this cavity by applying pressure via the helium fill line. This time, to make the data easier to interpret, only the amplitude of each measurement is shown ($|S11|$). The pressure is applied through a fill line, which is connected to a high pressure helium cylinder at room temperature. The fill line is slowly pressurized while the pressure is monitored through a gauge. When the desired pressure is reached, a valve is closed to isolate the helium reservoir from the pressurization circuit. This is repeated for each pressure measurement. The response of our cavity is shown in Fig. 2.8.

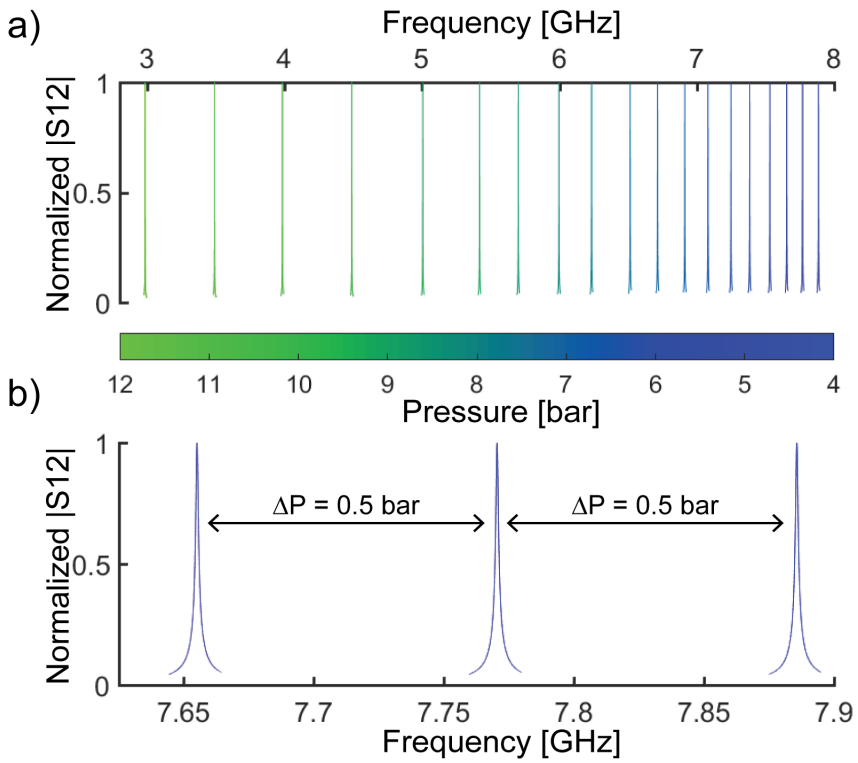

Figure 2.8: a) The normalized amplitude response of our cavity resonance as pressure is applied. Each Lorentzian response is separated by 0.5 bar.

Fitting each of these resonances in turn allows for the extraction of a quality factor and a resonance frequency for each applied pressure. This fitting procedure reveals that the cavity response to pressure is nonlinear, with the sensitivity becoming greater for large pressures, as expected from the expressions derived in section 1. The theoretical expectation for the cavity's response to pressure is overlaid in red. The results of this fitting procedure is outlined in Fig. 2.9.

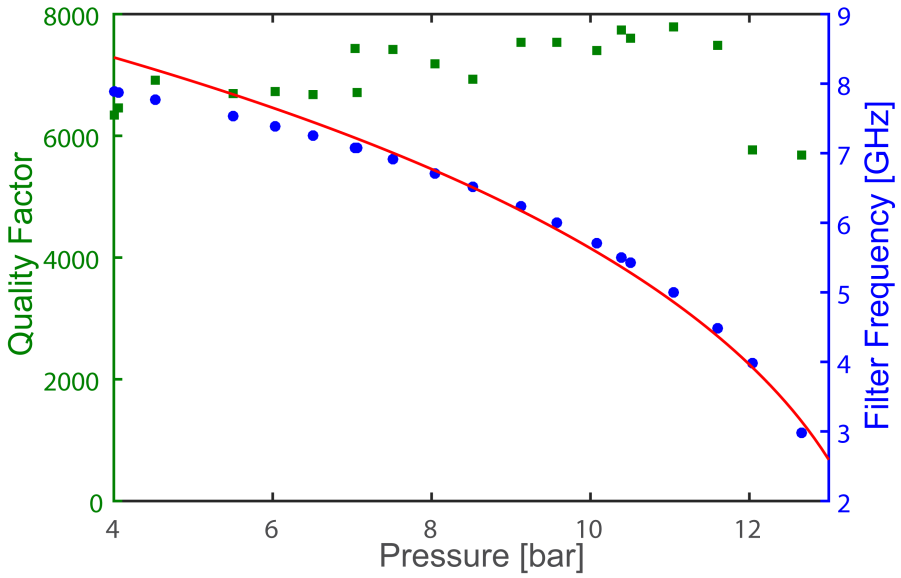

Figure 2.9: The resonance frequency and quality factor of our cavity as a function of applied pressure. Only minor degradation of the quality factor is evident over the entirety of the pressurization range. Overlaid in red is a fit to the theoretical expression, from which a sensitivity parameter is derived. The disagreement from the theory is discussed in the main text.

This fit allows us to extract an experimental value for both the responsivity parameter X, and the gap between the re-entrant stub and our membrane d. We find that the membrane has a responsivity of 7.3 μm/bar, and that the gap between the membrane and the stub is 100 μm, which is close to the design goal of 70 μm. It is worthy of note that the fit is imperfect. This imperfection likely comes from a deviation of the assumption of small membrane deflection in the deformation relation

for circularly clamped plates, and from the inaccuracy imparted from the small ratio of r_{cav}/l_m as described in Ref. [26].

2.9 Phase noise

One of the applications for a cavity of this type is the construction of a phase noise filter. Phase noise is a ubiquitous problem in any signal source, and causes a variety of problems ranging from errors in classical communication protocols such as phase shift keying [34], to causing unwanted heating in the measurement of an optomechanical system [35].

Phase noise is a deviation from the ideal sinusoid that manifests as a random function perturbing the phase of a sinusoidal signal:

$$V(t) = \cos(\omega t + \phi_o + \phi(t)). \tag{2.20}$$

This can be thought of as an instantaneous, time varying change to the frequency of the signal, which will be critical in understanding the measurement apparatus later in this chapter.

Phase noise can be pictured in the time and frequency domains follows. Note the apparent overall phase shift between the blue and red signals near the end of the trace. This is the total accumulated phase. One way of reducing the phase noise of a signal is to filter it. By applying a band pass filter centered in frequency space on the signal with phase noise, some of the noise can be rejected.

This filtration can be understood by consideration of the frequency response of the the resonator and of the signal generator. In the presence of phase noise, the power spectrum of the generator will be broadened with respect to a clean signal, as seen in Fig. 2.10. If the cavity is connected in transmission, then the cavity will reject noise outside of its linewidth, as pictured in Fig. 2.11.

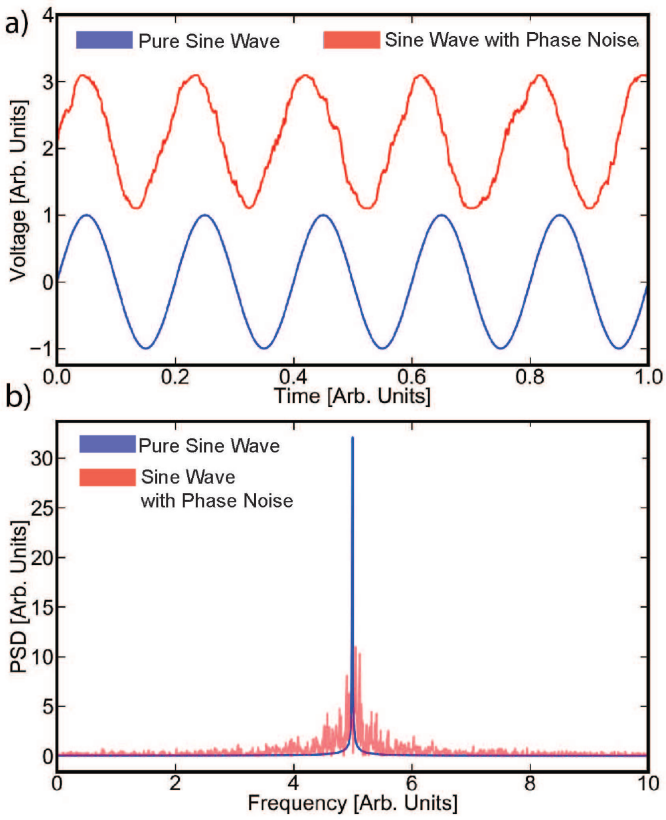

Figure 2.10: a) Sample signals demonstrating the effect of phase noise. The noise is modeled as a random perturbation to the phase at each time step b) Numerical Fourier transforms of the data presented in a, demonstrating the broadening effect of phase noise.

2.10 Phase Noise measurement

Although a variety of measurement schemes for phase noise exist, and are detailed in [36], this thesis will only outline the use of one of them: the delay line discriminator. This method was chosen due to its simplicity and the availability of equipment in conjunction with its commonplace and effective usage.

The delay line discriminator intuitively functions by splitting a noisy signal into two arms, then converting a phase noise into an absolute phase difference between the two arms through use of different path lengths. This phase difference is then measured with a mixer and a data acquisition card (DAQ). The details of this measurement

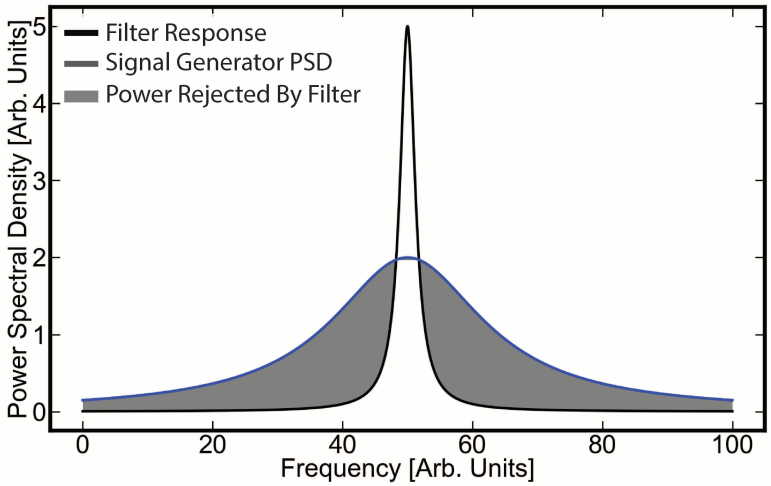

Figure 2.11: Graphical representation of the effect of a filter cavity. Outside of the linewidth of the cavity, power is reflected from the cavity instead of passed through it. This has the net effect of sharpening the spectral profile of the source, potentially significantly for high quality factor filters.

can be more completely understood by following the signal explicitly though the measurement path, as below.

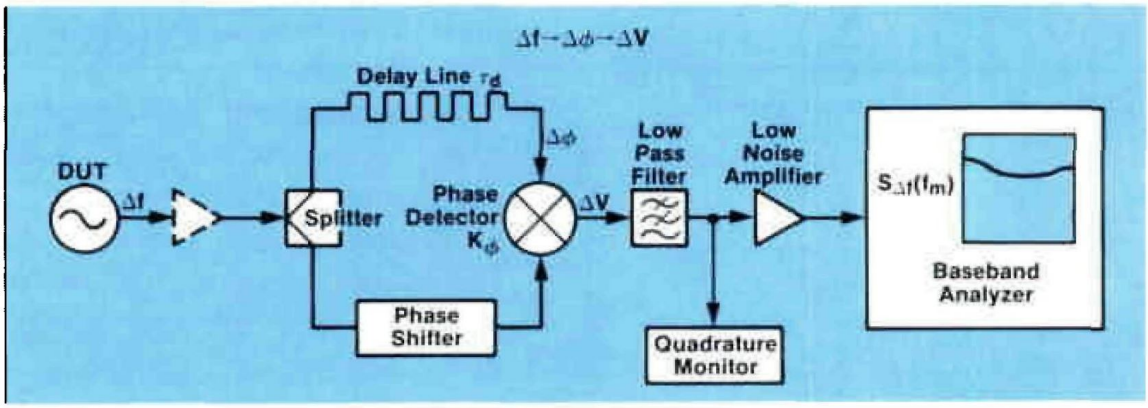

Figure 2.12: A schematic of the phase noise measurement scheme, taken from [36]. The following section will explicitly outline the signal as it travels through this diagram.

The first signal of interest in our measurement chain is the signal directly from the signal generator, here described as an entirely real function to facilitate the later

handling of the mixer, which acts only on the real part of a voltage signal.

2.10.1 Input Signal

$$V_s(t) = v_0 \cdot \cos\left(2\pi f_0 t + \frac{\Delta f}{f_m} \cdot \cos\left(2\pi f_m t\right)\right) \tag{2.21}$$

The signal is then split by a splitter:

2.10.2 Splitter Output

$$V_d(t) = V_s(t) = v \cdot \cos\left(2\pi f_0 t + \frac{\Delta f}{f_m} \cdot \cos(2\pi f_m t)\right) \tag{2.22}$$

Where I have denoted the voltage in the *signal arm* as V_s and the voltage in the *delay arm* as V_d. Directly after the splitter, these voltages are the same, with amplitude v.

2.10.3 Introduction of Delay

By design, one arm of the interferometer is made to be much longer than the other. This asymmetry develops a phase difference between the two arms. The larger the difference in length between the two arms, the larger the phase difference. Accounting for the added phase difference, the signals just before the mixer are:

$$V_s(t) = v \cdot \cos\left(2\pi f_0 t + \frac{\Delta f}{f_m} \cdot \cos(2\pi f_m t)\right) \tag{2.23}$$

$$V_d(t) = v \cdot \cos\left(2\pi f_0 \left(t - \tau_d\right) + \frac{\Delta f}{f_m} \cdot \cos\left(2\pi f_m \left(t - \tau_d\right)\right)\right) \tag{2.24}$$

2.10.4 Mixer Output

One can now employ a mixer in order to measure this phase difference. The sensitivity of the mixer is captured in the math by a constant K_ϕ which must be experimentally calibrated. Here is the output of the mixer:

$$V_m(t) = K_\phi \cdot \Bigg[\underbrace{\cos\left(2\pi f_0(t-\tau_d) + \frac{\Delta f}{f_m}\cos(2\pi f_m(t-\tau_d)) - 2\pi f_0 t - \frac{\Delta f}{f_m}\cos(2\pi f_m t)\right)}_{\text{difference frequency}} + \underbrace{\cos\left(2\pi f_0(t-\tau_d) + \frac{\Delta f}{f_m}\cos(2\pi f_m(t-\tau_d)) + 2\pi f_0 t + \frac{\Delta f}{f_m}\cos(2\pi f_m t)\right)}_{\text{sum frequency}} + \text{harmonics} \Bigg] \quad (2.25)$$

2.10.5 Filter Output

The information that we are looking for, although this is not obvious yet, is ensconced in the difference frequency term. This term can be isolated through the use of a low-pass filter. This filter is important not only to simplify analysis, but also to eliminate aliasing of the high frequency harmonics due to finite sampling time of the DAQ. If the filter is chosen such that only the difference frequency remains, then the output of the low pass filter is:

$$V_{\text{LPF}} = K_\phi \cdot \left(\cos\left(2\pi f_0(t-\tau_d)\right) + \frac{\Delta f}{f_m}\cos(2\pi f_m(t-\tau_d))) - 2\pi f_0 t - \frac{\Delta f}{f_m}\cos(2\pi f_m(t))\right). \quad (2.26)$$

We can now collect like terms and simplify the above to:

$$V_{\mathrm{LPF}} = K_\phi \cdot \left(\cos(-2\pi f_0 \tau_d) + 2\frac{\Delta f}{f_m} \sin(\pi f_m \tau_d) \sin(2\pi f_m (t - \tau_d/2)) \right). \tag{2.27}$$

2.10.6 Quadrature Assumption

If we introduce a phase shifter into the signal arm of the interferometer, as depicted in Fig. 2.12, we gain the freedom to easily tune the relative phase between the two arms. If we choose the two arms to be perfectly in quadrature (with noise being only small excursions from this phase relationship), a couple of convenient property emerges: the output voltage becomes linearly dependent on the phase, and the sensitivity to phase differences between the two arms is maximized. To see this more clearly, let us do a quick example.

Quadrature Demonstration

To see more clearly the utility in choosing the two arms to be in quadrature, let's momentarily dispense of the complicated notation of this section and just look at the multiplication of two sinusoids in quadrature:

$$\sin(\theta)\cos(\theta). \tag{2.28}$$

This can be re-written as

$$\frac{1}{2}\sin(2\theta), \tag{2.29}$$

and for small values of θ, this can be approximated as

$$\frac{1}{2}\sin(2\theta) \approx \theta. \tag{2.30}$$

In addition to this, setting the phases in quadrature makes the apparatus maximally sensitive to changes in phase between the two arms. This is hinted at in Eq. 1.27, but can be seen explicitly with only a little bit of extra machinery. Consider two sinusoids with an arbitrary phase difference:

$$\sin(\theta)\sin(\omega t + \phi) \tag{2.31}$$

This can be simplified as.

$$\sin(\omega t)\sin(\omega t + \phi) = \frac{\cos(2\omega t\phi) - \cos(\phi)}{2}. \tag{2.32}$$

In order to see the sensitivity maximum, we need to imagine this is acted on by a low pass filter, just as in the actual measurement setup

$$LPF[\sin(\omega t)\sin(\omega t + \phi)] = \frac{-\cos(\phi)}{2}. \tag{2.33}$$

Taking the derivative, yields

$$\frac{d}{d\phi}LPF[\sin(\omega t)\sin(\omega t + \phi)] = \frac{\sin(\phi)}{2}. \tag{2.34}$$

This is maximized when ϕ is 90°, implying the original sinusoids are in quadrature. These points together are the heart of why it is a useful thing to choose the phase in the arms to be in quadrature to one-another. The output becomes as close to linear as possible, and the sensitivity is maximized.

With this intuition in hand, let us return to the explicit calculation.

2.10.7 Mixer Inputs In Quadrature

By tuning the phase shifter in the signal arm, we can tune the two arms to be in quadrature. This is mathematically described by taking:

$$2\pi f_0 \tau_d = (2K+1)\frac{\pi}{2}, K\epsilon(1,2,3...). \tag{2.35}$$

Introducing this into our equation for the voltage and applying trigonometric identities to simplify yields the following equation for the voltage after the mixer:

$$V_{\text{Mixer}}^{\text{Quadrature}} = K_\phi \sin\left[2\frac{\Delta f}{f_m}\sin(\pi f_m \tau_d)\sin(2\pi f_m(t-\tau_d/2)\right]. \tag{2.36}$$

In practice, the quadrature assumption is satisfied by monitoring the DC part of the output of the low pass filter and adjusting the phase until this DC part is zero. K_ϕ is determined by finding the slope of this DC part as you change the phase.

2.10.8 Small Signal Assumption

We can make a final simplification to our above equations. In the case where the phase excursions are small, as would be expected in a commercial signal generator, we can make the usual small angle approximation for sinusoids: $\sin(\theta) \approx \theta$. This approximation leaves us with

$$V_{\text{Mixer}}^{\text{Quadrature}}(t) \approx 2K_\phi \frac{\Delta f}{f_m}\sin(\pi f_m \tau_d)\sin(2\pi f_m(t-\tau_d/2). \tag{2.37}$$

This is the final form of the voltage signal we read with our DAQ card.

2.10.9 Transfer Function

A powerful tool in interpreting the data being recorded on our DAQ is the system's transfer function. This is the function that describes the output of the system when it experiences an input at a given frequency.

The prefactors to the sinusoid in the previous equation are exactly this response. For an applied sinusoidal voltage with frequency f_M, the amplitude of the response will be those prefactors. Explicitly:

$$\Delta V \approx 2K_\phi \frac{\Delta f}{f_m} \sin(\pi f_m \tau_d). \tag{2.38}$$

This function can also be thought of in this context as the *sensitivity* of our system to phase noise. In order to interpret it most clearly, and to conform to convention, we choose to re-arrange this expression slightly:

$$\Delta V \approx 2K_\phi \pi \tau_d \Delta f \frac{\sin(\pi f_m \tau_d)}{\pi f_m \tau_d} = 2K_\phi \pi \tau_d \Delta f \mathrm{sinc}(\pi f_m \tau_D). \tag{2.39}$$

The first important thing to note about this function is that the sensitivity is not constant for all frequencies. In fact, the sensitivity goes to *zero* when $f_m \cdot \tau_d$ is an integer. This can cause serious issues in the accuracy of the reported phase noise if not handled appropriately.

This non-constant sensitivity can be addressed in two ways: most crudely, one could limit the measurement frequencies to a range where the sinc function is approximately 1. Mathematically, this condition is given by:

$$\pi \tau_d f_m \ll 1. \tag{2.40}$$

Physically, this corresponds to only measuring small frequencies of noise, or having an extremely short delay line, which directly reduces the sensitivity of the measurement. When this condition is satisfied, the transfer function reduces to

$$\Delta V \approx K_\phi 2\pi\tau_d \Delta f. \tag{2.41}$$

A more sophisticated approach involves accounting for the non-uniform, but known, sensitivity of the measurement apparatus and adjusting the measured voltage spectrum to reflect the changing sensitivity. Practically, this is achieved by calculating τ_d using the known difference in coaxial cable length between the two lines, and then dividing the apparent voltage spectrum by the known transfer function to acquire the true voltage spectrum. This is the approach taken in this work.

A set of labeled, normalized, transfer functions taking $\tau_d = 5$ μs , 1 μs are shown in Fig. 2.13 to make concrete the ideas introduced above.

2.11 Results

The results of our phase noise measurement are summarized in Fig. 2.14. In a) our aparatus is sketched, showing our physical implementation of the math described in this chapter.

From the results in section b), it can be seen that our tunable filter topology is capable of reducing the phase noise of a commercial signal generator by approximately 10 dB. The data indicates that the filtration begins to take effect $\approx$ 400 kHz from the carrier. This is consistent with the intuition that the filtration will take place outside of the cavity linewidth. Our cavity quality factor of $\sim$7000 implies a full width half max linewidth of:

$$\Delta f = \frac{f_0}{Q} = \frac{5\,\text{GHz}}{7000} \approx 715\,\text{kHz}. \tag{2.42}$$

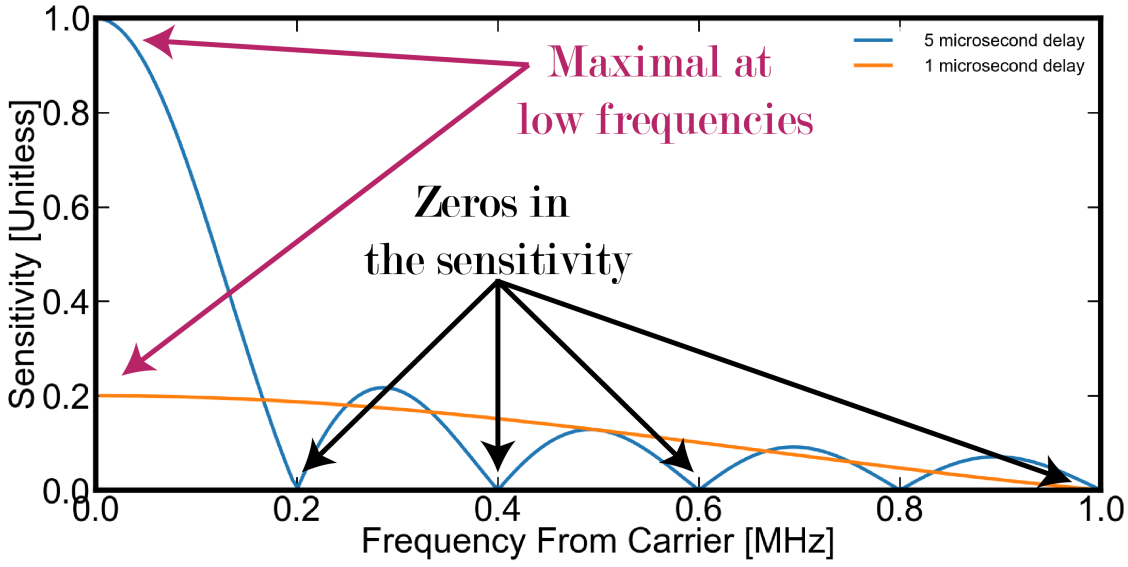

Figure 2.13: Two representative normalized transfer functions demonstrating the nature of the sensitivity of a delay line discriminator. They are normalized to the sensitivity of the 5 μs delay line, demonstrating the improved sensitivity for longer delay lines. At low frequencies, the sensitivity is flat and maximal, which can be used to justify approximating the sensitivity as a constant for small frequency ranges. It can be seen that the shorter delay line, while having reduced overall sensitivity, is flatter over a larger range.

We anticipate filtration to begin at around half of the full width from the carrier, or $f_{\text{filter}} \approx 357\,\text{Hz}$, consistent with visual inspection of Fig. 2.14.

2.12 Conclusion

In conclusion, we have here presented a tunable filter cavity with a novel, intrinsically cryogenically compatible tuning mechanism. The range of our tuning at cryogenic temperatures is an unprecedented 5 GHz. We have demonstrated that its quality factor does not degrade significantly over the entire course of tuning, and although the quality factor we present is modest, the literature suggests that this type of cavity's quality factor can be improved substantially through more the use of higher purity aluminium [1].

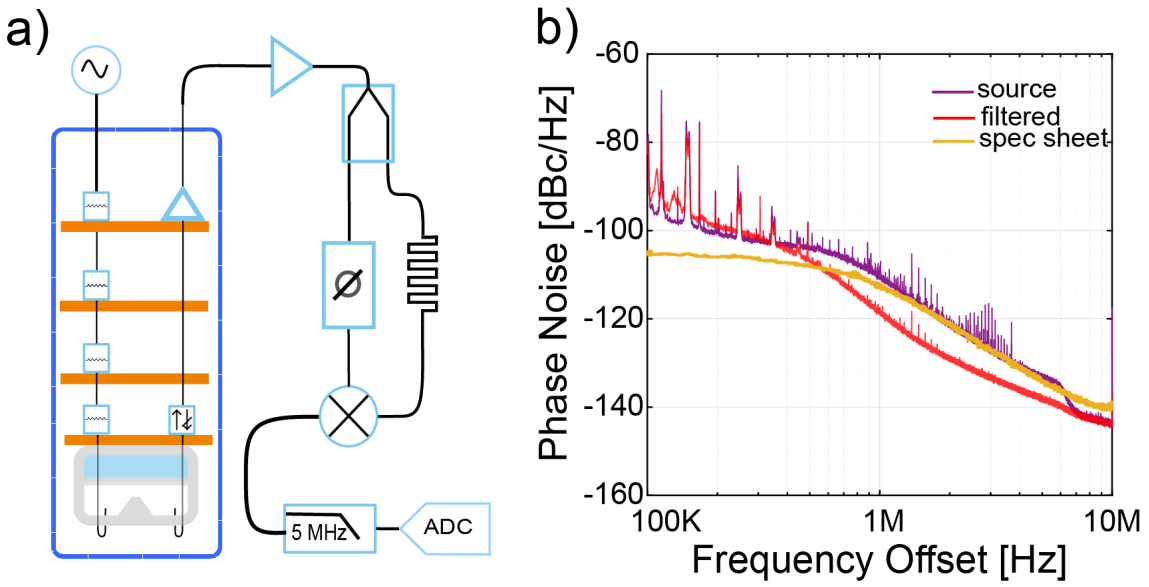

Figure 2.14: a) A schematic representation of our entire phase noise measurement apparatus, including the dilution refrigerator, the helium fill line, the cavity, and the delay line discriminator. b) Measurements of our source measured with no filtration, and then with the cavity phase noise filter in line. $\sim$ 10 dB of filtration is demonstrated from $\sim$ 400 kHz until the limit of our detection range.

Chapter 3

Microwave optomechanics

Cavity optomechanics, which at its core entails the cavity enhanced interaction of photons and phonons, has proven to be a powerful technique over the past decade. It has enabled such remarkable quantum experiments as ground-state cooling of mechanical resonators [37, 38], the entanglement of itinerant photons and localized phonons [39], the entanglement of two mechanical resonators [40], quantum-limited sensing [41], and even promises to allow for quantum nondemolition measurements of single phonons [42, 43, 44, 45], and conversion between single microwave photons and single telecom-wavelength photons [4, 5, 46]. One of the strengths of cavity optomechanics is that mechanical resonators can be coupled to a wide variety of electromagnetic cavities – motivating wavelength conversion applications – but most experiments have focused on GHz-frequency microwave cavities and telecom-wavelength optical cavities for practical reasons.

While remarkable experiments have been performed with telecom-wavelength optical cavities, microwave cavity optomechanics have two major advantages when it comes to experiments and applications in the quantum regime. First, the mechanical resonator in microwave optomechanics often incorporates a metallic layer, which allows for rapid thermalization to a cryogenic environment, even deep in the supercon-

ducting state. Second, many photons can be pumped into a microwave cavity without causing heating, in large part because of the remarkable properties of superconducting electronics, but also because the higher energy photons of telecom-wavelengths are easily absorbed into materials and cause significant heating, even at the single photon level. [43, 47, 48]

This chapter will describe the design, fabrication, and measurement of a microwave optomechanical system that exploits the dominant capacitance of a re-entrant cavity to couple with an aluminized silicon nitride membrane. I begin with a description of this system and a toy model describing the coupling between the microwave and mechanical elements. I then outline measurements of the microwave and mechanical properties of the system using a vector network analyser and microwave homodyne respectively. I continue by describing the calculation and finite element method simulations required to estimate the optomechanical coupling parameter. Finally, I show that the optomechanical coupling is sufficient to cool the mechanical element from its 450 mK environment to 160 mK using backaction cooling.

3.1 A Post Cavity Implementation

3.1.1 Microwave Cavity

The cavity chosen for the optomechanical study carried out here is the re-entrant cavity. Just as in the previous chapter, the re-entrant stub allows for the capacitance of the system to be localized in one area. The cavity was machined out of 6061 aluminium due to its low cost, availability of materials, ease of machining, and readily accessible superconducting transition temperature of 1.2 K. The outer radius of the cavity was chosen to fit the inner vacuum can of our closed-loop ^{3}He cryostat. The inner stub was chosen for ease of machining and to maximize overlap with the membrane above.

Additionally, as will be shown in the next section, optomechanical coupling is maximized for small gaps. For this reason, the stub was machined as close to the lid as possible. Nominally, this gap is 5 thousandths of an inch, which is the smallest increment on our milling machine.

3.1.2 Mechanical Resonator

The mechanical element in this system is an aluminium coated SiN membrane. The membrane is produced by depositing a 50 nm thick layer of SiN on top of a thick Si handle, then selectively etching away a window of Si to leave only the thin SiN suspended from the remaining Si handle. These membranes are sold commercially by Norcada in a variety of sizes.

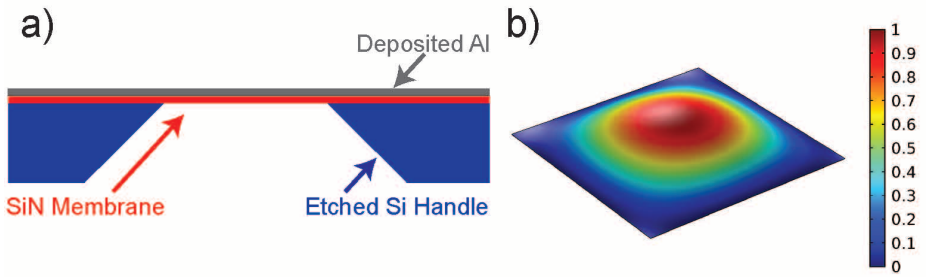

Figure 3.1: a) A cross-sectional schematic of the aluminized membrane. b) A COMSOL simulation of the lowest order mechanical mode of this membrane.

In order to couple the mechanical motion of the membrane and the microwave mode, the lid of the resonator had a small depression milled into it, and the chip was placed inside. To mechanically hold the chip in place, as well as to ensure that a continuous layer of metal could be deposited on the chip, a small amount of silver paste was applied to the face of the chip, bridging the gap between the faces of the lid and chip. This silver paste was cured at 200° C for 1 hour. Once the curing was complete, the entire lid was loaded into a sputtering machine and 50 nm of aluminium was sputtered on top of the entire lid. A schematic of our aluminized chip with a

COMSOL simulation of its lowest order mode is shown in Fig. 3.1. A photograph of the cavity is shown in Fig. 3.2.

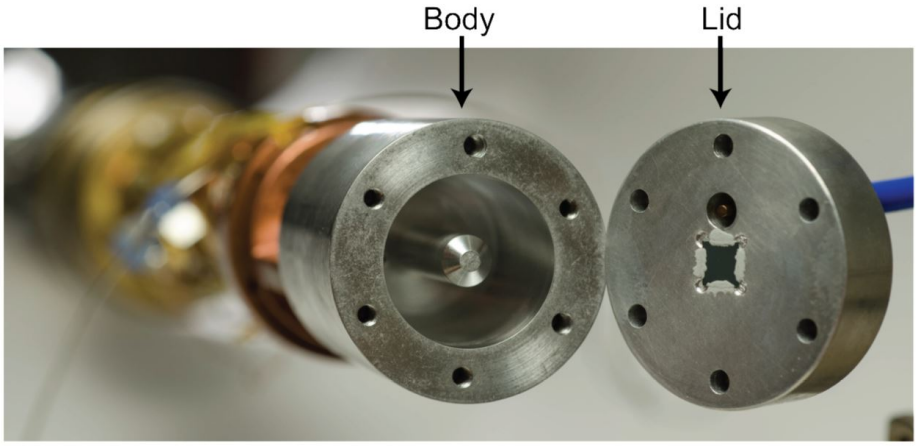

Figure 3.2: A photograph of the microwave cavity with the Norcada membrane recessed into the lid. Visible just above the chip is the antenna coupler used measure the microwave properties of the cavity.

To maximize the changing capacitance, and to allow for relatively large posts, a 2 mm x 2 mm membrane was chosen. Its large size loosens the alignment tolerances between the chip recession and the stub below.

3.2 Analytical Optomechanical Coupling for A Re-Entrant Membrane Cavity

The coupling for any type of cavity that has one dominant pliable capacitance can be analytically calculated as follows. First consider the expression for the resonant frequency of a microwave resonator:

$$\omega = \frac{1}{\sqrt{LC}}. \tag{3.1}$$

In our case, where the pliable capacitance dominates all other sources and is very nearly two parallel plates, C can be replaced with the formula for a parallel plate

capacitor:

$$C \approx \epsilon_0 \frac{A}{d}. \tag{3.2}$$

Now, we can derive an expression for the optomechanical coupling (G, the "frequency pull parameter") by modeling the motion of the pliable capacitor plate as a simple change in the distance between the two plates, here the stub and the lid. We can thus write $d = d_0 - x$, where d is the total gap between the lid and the body, d_0 is the gap with no deformation of the pliable element, and x is the distance travelled by the pliable element. Taking the derivative with respect to x yields:

$$\frac{\delta\omega}{\delta x} = G = \frac{\delta}{\delta x}\left(\frac{AL\epsilon_0}{d_0 - x}\right)^{-1/2} = -\frac{1}{2}\sqrt{\frac{1}{AL\epsilon_0(d_0 - x)}}. \tag{3.3}$$

If our system is undergoing small amplitude oscillations, we can simplify by considering the optomechanical coupling for only small excursions from equilibrium ($x \approx 0$)

$$G \approx -\frac{1}{2}\sqrt{\frac{1}{AL\epsilon_0(d_0 - x)}}\bigg|_{x=0} = -\frac{1}{2}\sqrt{\frac{1}{AL\epsilon_0 d_0}}. \tag{3.4}$$

This expression is sometimes re-arranged, using the formula for a parallel plate capacitance above as:

$$G \approx \frac{\omega}{2d}, \tag{3.5}$$

which is useful experimentally when one measures ω_c, but obfuscates the true $1/\sqrt{d_0}$ dependence on the gap size.

This derivation gives us an intuitive guide when designing systems such as these: the unperturbed gap between the plates of the pliable capacitor should be made as small as possible to maximize optomechanical coupling, consistent with the intuition derived in the previous chapter.

3.3 Refrigeration

Armed now with a description of the re-entrant cavity and its opotomechanical coupling, we can turn our attention to preparing it for measurement.

For this experiment, a closed loop ^{3}He system was used to cool the system down to a base temperature of ∼400 mK, considerably below the 1.2 K superconducting transition temperature of aluminium. Coaxial cables from Coax-Co Japan were used to carry signals from room our room temperature measurement equipment to the device and back. Pasternack Pe-034 connectors were used to connectorize the coax lines. No attenuation was used on the down due to heating issues that arose upon their inclusion. A Pasternack directional coupler was included before the cavity to reduce noise.

3.4 Cavity Characterization

This section will describe the measurements carried out to characterize the microwave and mechanical elements in our system.

3.4.1 Microwave Cavity Measurements

The system was first interrogated with a VNA to extract its microwave cavity parameters. As described in chapter 2, a VNA can be used to extract the scattering parameters of a microwave cavity, and these scattering parameters can be fit to extract the center frequency and the linewidth. These can be used to derive the quality factor. The data displayed in Fig. 3.3 demonstrates this process, and yields (κ, ω, Q) = (67 kHz, 1.8 GHz, 2.7 $\times 10^4$).

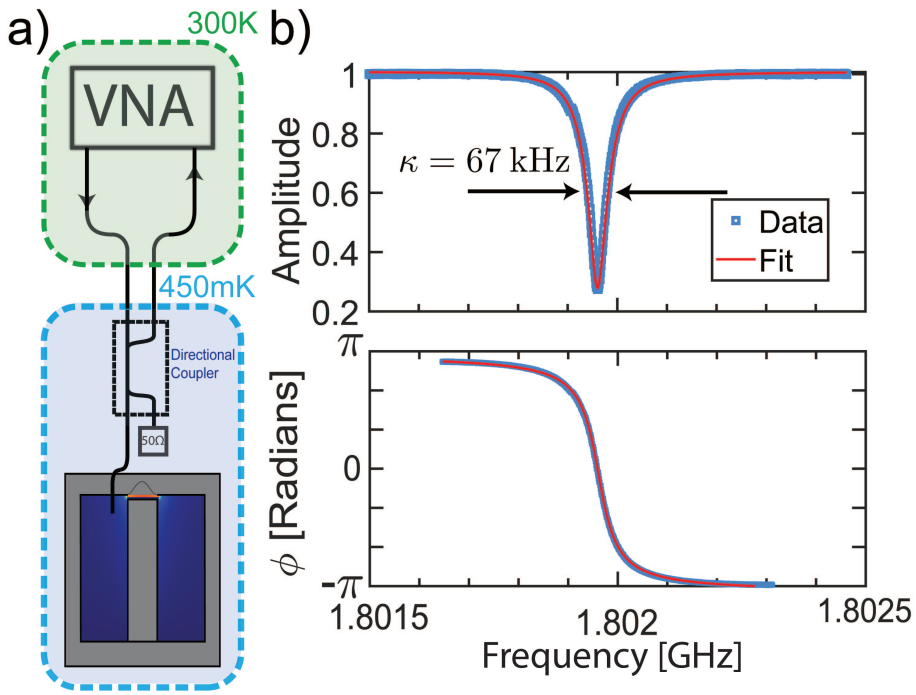

Figure 3.3: a) A schematic representation of the measurement apparatus used to determine the microwave cavity parameters. b) Scattering parameter data from the apparatus in a) with fits and the extracted linewidth overlaid.

3.4.2 Mechanical Measurements

With the microwave properties of the cavity understood, we turn our attention to the mechanical characteristics of the metallized SiN membrane. To measure the mechanical properties, we will do two very similar measurements, both exploiting a phase sensitive measurement scheme called microwave homodyne.

First, to locate the peak, we will sweep the frequency of a piezoelectric buzzer to drive the mechanical motion. When the frequency of the buzzer is the same as the mechanical resonance frequency of the Norcada membrane, the amplitude of its motion will become large, relaxing the noise floor requirements of our measurement. This is necessary because the deposition of aluminium has modified the resonance frequency.

Then, with the frequency of the mechanical resonance known, we will turn off the piezo and let the environmental thermal energy drive the mechanics. By using the known sensitivity of our measurement apparatus in conjunction with the known temperature of the resonator, we extract the optomechanical coupling coefficient.

Driven Mechanics

In order to most easily see the mechanics of the system, the system was strongly driven with a circular piezo buzzer. Although the piezo buzzer has a nominal resonance frequency of 9 kHz, dictated by its geometry, it still vibrates with significant amplitude at the frequencies of interest for this experiment. This type of measurement serves only to locate the mechanical resonance.

Thermomechanics

Once the piezo driven mechanics have been found, a natural next step is to look for the thermally driven motion of the mechanical resonator. This type of measurement allows us to determine the optomechanical coupling factor, G, through use of thermomechanical calibration [49].

Thermomechanical calibration begins with the noise spectrum for a linear optomechanical system [49]:

$$S_{\mathrm{VV}}(\omega) = S_{\mathrm{VV}}^{\mathrm{nf}} + \alpha \frac{4k_B T \Omega_m}{m_{\mathrm{eff}} Q} \cdot \frac{1}{(\Omega_m^2 - \omega^2)^2 + (\frac{\omega \Omega_m}{Q})^2}, \tag{3.6}$$

where $S_{\mathrm{VV}}(\omega)$ is the spectral density, $S_{\mathrm{VV}}^{\mathrm{nf}}$ is the spectral contribution of the noise floor, α is a conversion factor between a spectral density in units of meters and one in units of volts (which is dependent on the measurement apparatus), Ω_m is the mechanical resonance frequency, Q is the mechanical quality factor, and ω is the independent variable frequency. In the high Q limit, this can be approximated as a Lorentzian with center frequency determined by Ω_m and width determined by Q, but

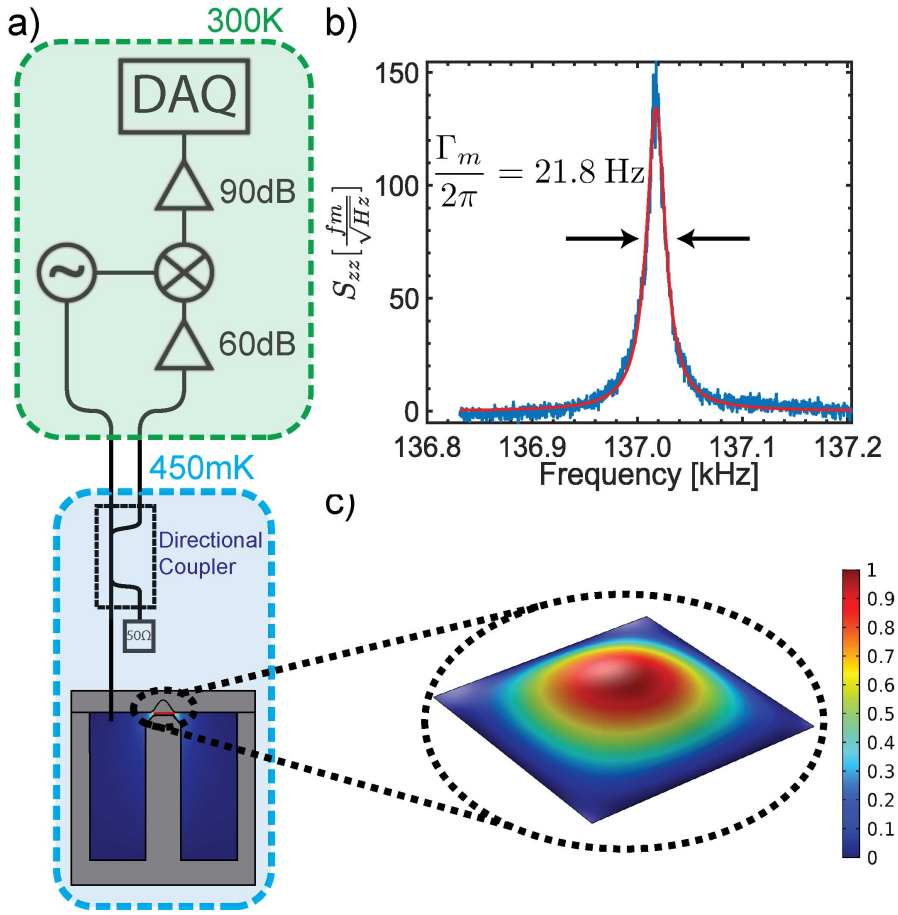

Figure 3.4: a) A schematic of the homodyne apparatus used to measure the mechanical parameters and the optomechanical coupling. b) Calibrated thermomechanical motion of the metallized SiN membrane at 450 mK taken using the homodyne apparatus of panel a. Fitting the thermomechanical motion allows extraction of the mechanical linewidth (21.8 Hz), the measurement noise floor (2.9 fm/$\sqrt{\text{Hz}}$), and the optomechanical coupling, $G/2\pi = 300$ Hz. c) A COMSOL simulation of the measured mechanical mode.

in this work this form is used. The only parameter that cannot be fit directly from thermomechanical data, α, can be expressed as:

$$\sqrt{\alpha} = \frac{\delta V}{\delta z}. \tag{3.7}$$

By applying the chain rule, and noting that $\frac{\delta\omega}{\delta z}$ is G, we can write:

$$\sqrt{\alpha} = \frac{\delta V}{\delta z} = \frac{\delta V}{\delta \omega}\frac{\delta \omega}{\delta z} = \frac{\delta V}{\delta \omega} \cdot g, \tag{3.8}$$

where we have introduced $\delta V/\delta\omega$ as the voltage sensitivity of the system to small changed in ω. This parameter can be measured experimentally by manually adjusting the phase shifter and approximating the slope at the measurement setpoint. This can be understood by recalling that a small change in the resonant frequency in a homodyne measurement apparatus results in no change in the magnitude of microwave power reflected from the cavity, but a large change in phase. This optomechanical phase shift can be mimicked with a phase shifter, and the voltage output of the mixer can be monitored to determine the experimental sensitivity. Carrying out this procedure on our homodyne system yields a sensitivity of 225 mV/radian.

The only remaining unknown, the last barrier before being able to assert G, is the effective mass of the resonator, m_{eff}. This mass can be determined with the help of a FEM solver like COMSOL. m_{eff} can be expressed as: [50]

$$m_{\text{eff}} = \int \rho |r(x)|^2 dV. \tag{3.9}$$

A fruitful assumption for thin membranes is that the density is constant over the thickness of the membrane. The integral can then be rewritten as

$$m_{\text{eff}} = \int \rho \cdot t |r(x)|^2 dA. \tag{3.10}$$

Breaking the integral into two subdomains of constant ρ (the membrane itself, and the aluminium coating it), and assuming the density of SiN and Al are constant over their respective areas of integration, yields:

$$m_{eff} = (\rho_{\text{SiN}} \cdot t_{\text{SiN}} + \rho_{\text{Al}} \cdot t_{\text{Al}}) \cdot \int |r(x)|^2 dA. \tag{3.11}$$

All that remains is to actually carry out the integral in COMSOL, which is done using the built-in integration functions. A screenshot detailing the salient features of the COMSOL simulation is shown in Fig. 3.5. Via this method, for a 2 mm x 2 mm

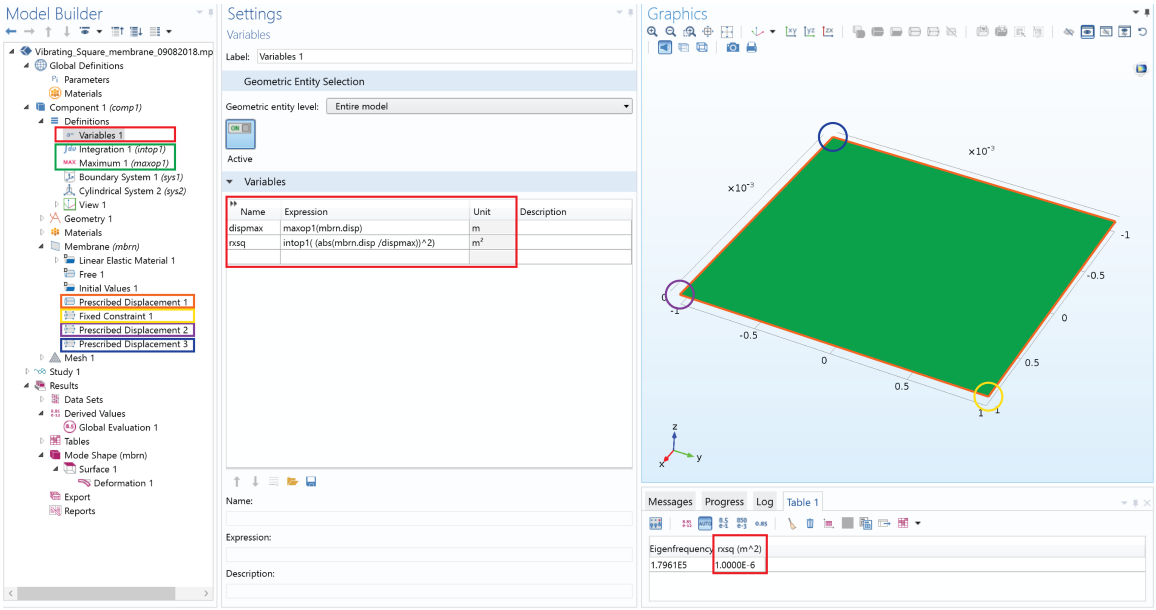

Figure 3.5: A screenshot depicting the required elements to determine effective mass in COMSOL. Membrane physics are used. Boxed in red are the components related to defining *variables* in COMSOL, which are the entities require the evaluation of an integral or a maximum over the domain of interest. In orange, purple, yellow, blue are the boundary conditions. Orange sets the z displacement to be zero. Purple and blue set the x and z to be zero respectively.

membrane, 50 nm thick, with 50 nm of aluminium deposited on it, it is found that $|r(x)|^2 = 1 \times 10^{-6}\text{m}^2$ and that m_{eff}= 2916 ng.

Assuming that the temperature of the mechanical element is the same as the temperature of the cryostat, which is justified for low microwave drive power, we can now carry out a fit using Eq. 4.1 and determine G. This fit is shown in Fig. 3.4, and the corresponding G is 300 Hz/nm.

A related figure of merit for optomechanical systems is the *single photon* optomechanical coupling, g_0. It is expressed in terms of G as

$$g_0 = G \cdot x_{\text{ZPF}}, \tag{3.12}$$

where x_{ZPF} is the zero point fluctuation of the mechanical oscillator, given by

$$x_{\mathrm{ZPF}} = \sqrt{\frac{\hbar}{2m_{\mathrm{eff}}\Omega_{\mathrm{m}}}}. \tag{3.13}$$

Using the cavity paramters solved for above and these new equations, we can determine $(x_{\mathrm{ZPF}}, g_0) = (145 \text{ am}, 4.3 \times 10^{-5} \text{ Hz})$.

3.5 Optomechanical Cooling

Now that the cavity is fully characterized, we can leverage the optomechanical interaction to cool the mechanical resonator. When we apply a tone on the red-detuned sideband, the system will undergo an absorption process that preferentially robs energy from the mechanical oscillator and causes it to cool down [35]. This can be envisioned classically as a radiation pressure force that is always out of phase with the mechanical motion. Using the language of quantum mechanics, this is a preferential scattering of the drive photons into the cavity; a process that requires the absorption of a phonon, and thus the cooling of the mechanical mode. Increasing the power of the off-resonant tone increases the amount of cooling.

In order to quantify the amount of cooling, we start by noting that the process of cooling described above can be thought of as an additional source of damping on the membrane. The total damping is the sum of the intrinsic damping, Γ_m, and the damping imparted by the intra-cavity microwave field, Γ_{opt}:

$$\Gamma_{\mathrm{eff}} = \Gamma_m + \Gamma_{\mathrm{opt}}. \tag{3.14}$$

By characterizing the intrinsic mechanical linewidth at low microwave power, then observing how the linewidth changes as the power is increased, one can extract the optical damping at a given microwave power.

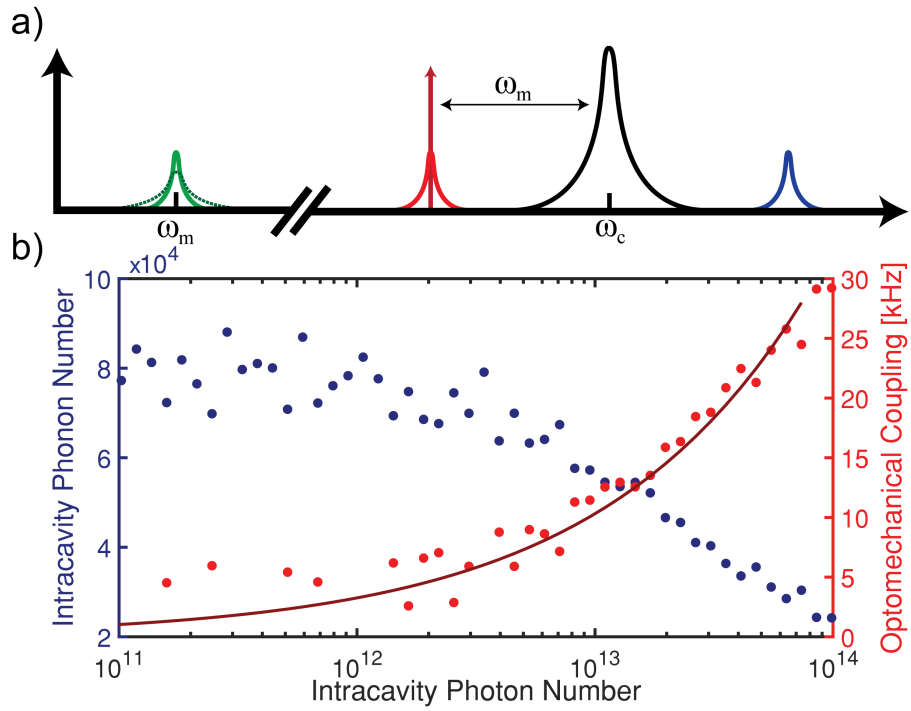

Figure 3.6: a) A schematic representation of the frequency spectrum present in our cavity optomechanical system. Our microwave resonance at ω_c is in black, with sidebands (red and blue) generated by interaction with the mechanical resonance (green). To implement radiation pressure cooling of the mechanical mode, we apply a pump tone to the red side of the microwave resonance, i.e. on the low-energy mechanical sideband. These red pump photons scatter with a mechanical phonon and are upconverted to ω_c, which is manifested as a broadening of the mechanical resonance. b) Increasing the power in the red pump tone increases the scattering rate and hence the cooling of the mechanical mode, as well as enhancing the optomechanical coupling rate. A fit to the coupling rate allows the extraction of $G/2\pi = 540$ Hz/nm).

Additionally, one can use the known total and external loss rates to determine the intracavity photon number given an input power using [51]:

$$\overline{n_{\text{cav}}} = \frac{P_{\text{in}}}{\hbar\omega}\frac{\kappa_e}{\Delta^2 + \kappa^2/4}. \tag{3.15}$$

Now, we can use this extracted optical damping rate and intracavity photon number to find the optomechanical coupling coefficient. In general, we have [51]:

$$\Gamma_{\text{opt}} = \frac{\kappa}{\kappa^2/4 + (\Delta + \Omega_m)^2} - \frac{\kappa}{\kappa^2/4 + (\Delta - \Omega_m)^2}. \tag{3.16}$$

Simplifying for the case where the applied tone is on the red sideband ($\Delta = -\Omega_m$)

$$\Gamma_{\text{opt}} = \frac{\kappa}{\kappa^2/4} - \frac{\kappa}{\kappa^2/4 + (2\Omega_m)^2}, \tag{3.17}$$

and further simplifying given that we are in the resolved sideband regime ($\Omega \gg \kappa$)

$$\Gamma_{\text{opt}} = \frac{4\overline{n_{cav}}g_0^2}{\kappa} = \frac{4G^2}{\kappa}. \tag{3.18}$$

Now that we have the cavity enhanced G, we can follow the same procedure we used in section 3.4.2, but now taking G as an input and solving for the temperature. This temperature can be converted into a number of intracavity phonons by using the measured mechanical resonance frequency and noting that the phonons follow Bose-Einstein statistics:

$$n_{\text{phonons}} = \frac{1}{e^{\hbar\omega/k_bT} - 1}. \tag{3.19}$$

The results of this procedure are summarized in Fig. 3.6, where I demonstrate cooling down to a temperature of 160 mK corresponding to a phonon occupancy of $2.4 \cdot 10^4$. It is worth noting that the derived value for G in strong disagreement with the value derived from fitting the calibrated mechanical data. This disagreement likely stems from the approximations used in deriving our formula (we are not deeply sideband resolved) as well as other effects such as absorptive heating at high microwave drive power.

3.6 Conclusion

In this chapter I described the design, fabrication, and measurement of a microwave optomechanical device consisting of an aluminium re-entrant microwave cavity coupled to a metalized SiN membrane. Through determining the scattering parameters

with a VNA and fitting them to theory, I show that the microwave cavity parameters are $(\kappa/2\pi, \omega/2\pi, Q) = (67$ kHz, 1.8 GHz, 2.7 $\times 10^4)$. Then, by doing a microwave homodyne measurement, I characterize the mechanical properties. I find that the aluminized membrane has its first mechanical resonance at $\omega/2\pi$ =137 kHz and its linewidth is $\Gamma_m/2\pi = 21.8$ Hz, corresponding to a mechanical quality factor of 6×10^3 I use this mechanical measurement in conjunction with a finite element simulation to extract the optomechanical coupling coefficient, which is $G = 300$Hz/nm. Finally, I demonstrate that this system can be back-action cooled from the 450 mK base temperature of our fridge down to 160 mK.

Chapter 4

Conclusion

4.1 Summary

The primary focus of this thesis was to present some recent work in applying re-entrant microwave cavities for use in a variety of systems. It summarized and explained the findings presented in [52], where a novel tuning mechanism involving a pressurized helium cavity was employed to produce microwave cavity tunabilities of more than 5 GHz without significant reduction in cavity quality factor. This represents the state of the art for cryogenic tunability of microwave cavities. Although the quality factor presented is significantly lower than what has been described in literature for comparable geometries [1], there are straightforward avenues of improvement to match this standard such as careful cavity surface treatment or the use of high purity aluminium.

It went on to describe an optomechanical system consisting of an aluminium coated silicon nitride membrane coupled capacitively to a similar microwave cavity. This optomechanical coupling permits measurement of the mechanical modes of the membrane, as well as the calibrated measurement of the optomechanical coupling. Although the optomechanical coupling is modest, it is sufficient to demonstrate

optomechanical cooling via the application of drive tones detuned from the optical resonance. This is demonstrated and compared to theory.

4.2 Next Steps

A straightforward avenue to improve the phase noise filter is to raise its quality factor. As aforementioned, this can be pursued through more careful machining and surface treatments. Following this improvement, the tool is ready for application, although the complexity of construction and implementation will likely dissuade users unless very sharp and precise filtering is an absolute necessity for multiple experiments.

The optomechanical system could be improved through more careful galvanic coupling between the chip's metalized face and the cavity lid. This would improve the microwave and mechanical quality factors as well as the optomechanical coupling, allowing for stronger sideband cooling.

The system, however, intrinsically has what I believe to be a killer defect: the optomechanical coupling factor is defined exclusively by the gap size between the stub and the lid. Careful and patient machining could reduce the gap from what we have presented here, but the techniques of microfabrication are better suited to producing small gaps, and thus large optomechanical couplings, even in 3D macroscopic cavities [2, 53].

Microwave cavities have been shown to be indispensable tools in modern science both for fundamental research and in the generation of new applications. There's no doubt in my mind that they will continue to play a part in the development of beautiful and interesting devices for a variety of purposes many years into the future.

Bibliography

[1] Matthew Reagor, Wolfgang Pfaff, Christopher Axline, Reinier W. Heeres, Nissim Ofek, Katrina Sliwa, Eric Holland, Chen Wang, Jacob Blumoff, Kevin Chou, Michael J. Hatridge, Luigi Frunzio, Michel H. Devoret, Liang Jiang, and Robert J. Schoelkopf. Quantum memory with millisecond coherence in circuit qed. *Phys. Rev. B*, 94:014506, Jul 2016.

[2] GA Peterson, S Kotler, F Lecocq, K Cicak, XY Jin, RW Simmonds, J Aumentado, and JD Teufel. Ultrastrong parametric coupling between a superconducting cavity and a mechanical resonator. *arXiv preprint arXiv:1906.11353*, 2019.

[3] R. Hisatomi, A. Osada, Y. Tabuchi, T. Ishikawa, A. Noguchi, R. Yamazaki, K. Usami, and Y. Nakamura. Bidirectional conversion between microwave and light via ferromagnetic magnons. *Phys. Rev. B*, 93:174427, May 2016.

[4] Reed W Andrews, Robert W Peterson, Tom P Purdy, Katarina Cicak, Raymond W Simmonds, Cindy A Regal, and Konrad W Lehnert. Bidirectional and efficient conversion between microwave and optical light. *Nature Physics*, 10(4):321, 2014.

[5] Amit Vainsencher, KJ Satzinger, GA Peairs, and AN Cleland. Bi-directional conversion between microwave and optical frequencies in a piezoelectric optomechanical device. *Applied Physics Letters*, 109(3):033107, 2016.

[6] M. J. Hill, R. W. Ziolkowski, and J. Papapolymerou. A high-q reconfigurable planar ebg cavity resonator. *IEEE Microwave and Wireless Components Letters*, 11(6):255–257, June 2001.

[7] Xiao Yu, Weibin Xi, and Songtao Wu. A 15-pole high temperature superconductor filter for radar applications. *Superconductor Science and Technology*, 31(6):065007, may 2018.

[8] Sormeh Setoodeh, Raafat R. Mansour, and D Gupta. Multi-layer low temperature superconducting k-band filter and diplexer design. *IEEE MTT-S International Microwave Symposium digest. IEEE MTT-S International Microwave Symposium*, pages 1–4, 06 2013.

[9] Lafe Spietz, John Teufel, and RJ Schoelkopf. A twisted pair cryogenic filter. *arXiv preprint cond-mat/0601316*, 2006.

[10] Hendrik Bluhm and Kathryn A. Moler. Dissipative cryogenic filters with zero dc resistance. *Review of Scientific Instruments*, 79(1):014703, 2008.

[11] Harold Weinstock and Martin Nisenoff. *Microwave superconductivity*, volume 375. Springer Science & Business Media, 2012.

[12] Sormeh Setoodeh. Superconducting microwave filters. Master's thesis, University of Waterloo, 2011.

[13] Sara Attar, Sormeh Setoodeh, Paul Laforge, Maher Bakri-Kassem, and Raafat R. Mansour. Low temperature superconducting tunable bandstop resonator and filter using superconducting rf mems varactors. *Applied Superconductivity, IEEE Transactions on*, 24:1–9, 08 2014.

[14] D. Peroulis, S. Pacheco, K. Sarabandi, and L. P. B. Katehi. Tunable lumped components with applications to reconfigurable mems filters. In *2001 IEEE MTT-S International Microwave Sympsoium Digest (Cat. No.01CH37157)*, volume 1, pages 341–344 vol.1, May 2001.

[15] H. Joshi, H. H. Sigmarsson, S. Moon, D. Peroulis, and W. J. Chappell. High-*q*fully reconfigurable tunable bandpass filters. *IEEE Transactions on Microwave Theory and Techniques*, 57(12):3525–3533, Dec 2009.

[16] H. Joshi, H. H. Sigmarsson, D. Peroulis, and W. J. Chappell. Highly loaded evanescent cavities for widely tunable high-q filters. In *2007 IEEE/MTT-S International Microwave Symposium*, pages 2133–2136, June 2007.

[17] M. Abdelfattah and D. Peroulis. High-q tunable evanescent-mode cavity siw resonators and filters with contactless tuners. *IEEE Transactions on Microwave Theory and Techniques*, pages 1–12, 2019.

[18] N. Carvalho, Y. Fan, J-M. Le Floch, and M. Tobar. Piezoelectric voltage coupled reentrant cavity resonator. *Rev. Sci. Instrum.*, 85:104705, 2014.

[19] N. C. Carvalho, Y. Fan, and M. E. Tobar. Piezoelectric tunable microwave superconducting cavity. *Rev. Sci. Instrum.*, 87:094702, 2016.

[20] M. Stammeier, S. Garcia, and A. Wallraff. Applying electric and magnetic field bias in a 3d superconducting waveguide cavity with high quality factor. *arXiv:1712.08631*, 2018.

[21] J-M. Le Floch, Y. Fan, M. Aubourg, D. Cros, N. Carvalho, Q. Shan, J. Bourhill, E. Ivanov, G. Humbert, V. Madrangeas, and M. Tobar. Rigorous analysis of highly tunable cylindrical transverse magnetic mode re-entrant cavities. *Rev. Sci. Instrum.*, 84:125114, 2013.

[22] Xiaoguang L., L.. Katehi, W. Chappell, and D. Peroulis. High-q tunable microwave cavity resonators and filters using soi-based rf mems tuners. *Journal of Microelectromechanical Systems*, 19:774, 2010.

[23] Andrew M. Sessler and Simon S. Yu. Relativistic klystron two-beam accelerator. *Phys. Rev. Lett.*, 58:2439–2442, Jun 1987.

[24] David M Pozar. *Microwave engineering*. John Wiley & Sons, 2009.

[25] R. Heeres, P. Reinhold, N. Ofek, L. Frunzio, L. Jiang, M. Devoret, and R. Schoelkopf. Implementing a universal gate set on a logical qubit encoded in an oscillator. *Nat. Commun.*, 8:94, 2017.

[26] K. Fujisawa. General treatment of klystron resonant cavities. *IRE Transactions on Microwave Theory and Techniques*, 6:344, 1958.

[27] W. Young and R. Budnyas. *Roark's Formulas for Stress and Strain*. McGraw-Hill, New York, 2017.

[28] M. Reagor. *Superconducting cavities for circuit quantum electrodynamics*. Yale University, New Haven, 2016.

[29] M. S. Khalil, M. J. A. Stoutimore, F. C. Wellstood, and K. D. Osborn. An analysis method for asymmetric resonator transmission applied to superconducting devices. *Journal of Applied Physics*, 111(5):054510, 2012.

[30] Kevin D McKinstry and Carl E Patton. Methods for determination of microwave cavity quality factors from equivalent electronic circuit models. *Review of Scientific Instruments*, 60(3):439–443, 1989.

[31] S. Probst, F Song, P Bushev, A Ustinov, and M Weides. Efficient and robust analysis of complex scattering data under noise in microwave resonators. *Rev. Sci. Instrum.*, 86:024706, 2015.

[32] M.R. Abdul-Gaffoor A.A. Kishk D. Kajfez, S. Chebolu. Uncertainty analysis of the transmission-type measurement of q-factor. *Transaction on Microwave Theory and Techniques*, 47(3):367–371, 1999.

[33] MC Sanchez, E Martin, and JM Zamarro. Unified and simplified treatment of techniques for characterising transmission, reflection or absorption resonators. *IEE Proceedings H (Microwaves, Antennas and Propagation)*, 137(4):209–212, 1990.

[34] J. Proakis and Masoud Salehi. *Digital Communications*. McGraw-Hill, New York, 2007.

[35] A. Schliesser, R. Rivière, G. Anetsberger, and O. Arcizet. Resolved-sideband cooling of a micromechanical oscillator. *Nat. Phys.*, 4:415, 2008.

[36] Hewlett Packard. Phase noise characterization of microwave oscillators, frequency discriminator method. *HP Product Note 11729C-2*, 1985.

[37] JD Teufel, T. Donner, J.and Allman M. Li, D.and Harlow, K. Cicak, A. Sirois, J. Whittaker, K. Lehnert, and R. Simmonds. Sideband cooling of micromechanical motion to the quantum ground state. *Nature*, 475:359, 2011.

[38] Jasper Chan, TP Mayer Alegre, Amir H Safavi-Naeini, Jeff T Hill, Alex Krause, Simon Gröblacher, Markus Aspelmeyer, and Oskar Painter. Laser cooling of a nanomechanical oscillator into its quantum ground state. *Nature*, 478(7367):89, 2011.

[39] TA Palomaki, JD Teufel, RW Simmonds, and KW Lehnert. Entangling mechanical motion with microwave fields. *Science*, 342(6159):710–713, 2013.

[40] Ralf Riedinger, Andreas Wallucks, Igor Marinković, Clemens Löschnauer, Markus Aspelmeyer, Sungkun Hong, and Simon Gröblacher. Remote quantum entanglement between two micromechanical oscillators. *Nature*, 556(7702):473, 2018.

[41] PH Kim, BD Hauer, C Doolin, F Souris, and JP Davis. Approaching the standard quantum limit of mechanical torque sensing. *Nature communications*, 7:13165, 2016.

[42] Adil A Gangat, Tom M Stace, and Gerard J Milburn. Phonon number quantum jumps in an optomechanical system. *New Journal of Physics*, 13(4):043024, 2011.

[43] B. D. Hauer, A. Metelmann, and J. P. Davis. Phonon quantum nondemolition measurements in nonlinearly coupled optomechanical cavities. *Phys. Rev. A*, 98:043804, Oct 2018.

[44] Jeremie J Viennot, Xizheng Ma, and Konrad W Lehnert. Phonon-number-sensitive electromechanics. *Physical review letters*, 121(18):183601, 2018.

[45] Patricio Arrangoiz-Arriola, E Alex Wollack, Zhaoyou Wang, Marek Pechal, Wentao Jiang, Timothy P McKenna, Jeremy D Witmer, and Amir H Safavi-Naeini. Resolving the energy levels of a nanomechanical oscillator. *arXiv preprint arXiv:1902.04681*, 2019.

[46] AP Higginbotham, PS Burns, MD Urmey, RW Peterson, NS Kampel, BM Brubaker, G Smith, KW Lehnert, and CA Regal. Harnessing electro-optic correlations in an efficient mechanical converter. *Nature Physics*, 14(10):1038, 2018.

[47] Justin D Cohen, Seán M Meenehan, Gregory S MacCabe, Simon Gröblacher, Amir H Safavi-Naeini, Francesco Marsili, Matthew D Shaw, and Oskar Painter. Phonon counting and intensity interferometry of a nanomechanical resonator. *Nature*, 520(7548):522, 2015.

[48] G Goltsman, A Korneev, A Divochiy, O Minaeva, M Tarkhov, N Kaurova, V Seleznev, B Voronov, O Okunev, A Antipov, et al. Ultrafast superconducting single-photon detector. *Journal of modern optics*, 56(15):1670–1680, 2009.

[49] C. Doolin, B. D. Hauer, P. H. Kim, A. J. R. MacDonald, H. Ramp, and J. P. Davis. Nonlinear optomechanics in the stationary regime. *Phys. Rev. A*, 89:053838, May 2014.

[50] B.D. Hauer, C. Doolin, K.S.D. Beach, and J.P. Davis. A general procedure for thermomechanical calibration of nano/micro-mechanical resonators. *Annals of Physics*, 339:181 – 207, 2013.

[51] Markus Aspelmeyer, Tobias J Kippenberg, and Florian Marquardt. Cavity optomechanics. *Reviews of Modern Physics*, 86(4):1391, 2014.

[52] T. J. Clark, V. Vadakkumbatt, F. Souris, H. Ramp, and J. P. Davis. Cryogenic microwave filter cavity with a tunability greater than 5 GHz. *Review of Scientific Instruments*, 89(11):114704, 2018.

[53] Mingyun Yuan, Martijn A. Cohen, and Gary A. Steele. Silicon nitride membrane resonators at millikelvin temperatures with quality factors exceeding 108. *Appl. Phys. Lett.*, 107:263501, 2015.